

Identification of Melt Ponds in 2011 Summer Multi-year Pack Ice of the Canadian Beaufort Sea with Helicopter-Borne Laser, Ground-Penetrating Radar and Video

S.J. Prinsenbergh, I.K. Peterson, L. Lalumiere and J.S. Holladay

Ocean and Ecosystem Sciences Division
Maritimes Region
Fisheries and Oceans Canada

Bedford Institute of Oceanography
P.O. Box 1006
Dartmouth, Nova Scotia
Canada B2Y 4A2

2014

**Canadian Technical Report of
Hydrography and Ocean Sciences 299**



Fisheries and Oceans
Canada

Pêches et Océans
Canada

Canada

Canadian Technical Report of Hydrography and Ocean Sciences

Technical reports contain scientific and technical information of a type that represents a contribution to existing knowledge but which is not normally found in the primary literature. The subject matter is generally related to programs and interests of the Oceans and Science sectors of Fisheries and Oceans Canada.

Technical reports may be cited as full publications. The correct citation appears above the abstract of each report. Each report is abstracted in the data base *Aquatic Sciences and Fisheries Abstracts*.

Technical reports are produced regionally but are numbered nationally. Requests for individual reports will be filled by the issuing establishment listed on the front cover and title page.

Regional and headquarters establishments of Ocean Science and Surveys ceased publication of their various report series as of December 1981. A complete listing of these publications and the last number issued under each title are published in the *Canadian Journal of Fisheries and Aquatic Sciences*, Volume 38: Index to Publications 1981. The current series began with Report Number 1 in January 1982.

Rapport technique canadien sur l'hydrographie et les sciences océaniques

Les rapports techniques contiennent des renseignements scientifiques et techniques qui constituent une contribution aux connaissances actuelles mais que l'on ne trouve pas normalement dans les revues scientifiques. Le sujet est généralement rattaché aux programmes et intérêts des secteurs des Océans et des Sciences de Pêches et Océans Canada.

Les rapports techniques peuvent être cités comme des publications à part entière. Le titre exact figure au-dessus du résumé de chaque rapport. Les rapports techniques sont résumés dans la base de données *Résumés des sciences aquatiques et halieutiques*.

Les rapports techniques sont produits à l'échelon régional, mais numérotés à l'échelon national. Les demandes de rapports seront satisfaites par l'établissement auteur dont le nom figure sur la couverture et la page de titre.

Les établissements de l'ancien secteur des Sciences et Levés océaniques dans les régions et à l'administration centrale ont cessé de publier leurs diverses séries de rapports en décembre 1981. Vous trouverez dans l'index des publications du volume 38 du *Journal canadien des sciences halieutiques et aquatiques*, la liste de ces publications ainsi que le dernier numéro paru dans chaque catégorie. La nouvelle série a commencé avec la publication du rapport numéro 1 en janvier 1982.

Canadian Technical Report of
Hydrography and Ocean Sciences 299

2014

IDENTIFICATION OF MELT PONDS IN 2011 SUMMER MULTI-YEAR PACK ICE
OF THE CANADIAN BEAUFORT SEA WITH HELICOPTER-BORNE LASER,
GROUND-PENETRATING RADAR AND VIDEO

by

Simon J. Prinsenber, Ingrid K. Peterson, Louis Lalumiere¹ and J. Scott Holladay²

Ocean and Ecosystem Sciences Division
Maritimes Region
Fisheries and Oceans Canada
Bedford Institute of Oceanography
P.O. Box 1006
Dartmouth, N.S., B2Y 4A2

¹ Sensors by Design Ltd., 100 Peevers Crescent,
Newmarket, Ontario, L3Y 7T1

² Geosensors Inc., 66 Mann Ave.,
Toronto, Ontario, M4S 2Y3

© Her Majesty the Queen in Right of Canada, 2014.
Cat. No. Fs97-18/299E-PDF ISBN 978-1-100-24398-6 ISSN 1488-5417

Correct citation for this publication:

Prinsenberg, S.J., I.K. Peterson, L. Lalumiere and J.S. Holladay, 2014. Identification of melt ponds in 2011 summer Multi-Year pack ice of the Canadian Beaufort Sea with helicopter-borne Laser, Ground-Penetrating Radar and Video. Can. Tech. Rep. Hydrogr. Ocean Sci. 299: vi+65pp.

TABLE OF CONTENTS

Abstract	v
Résumé	vi
1.0 Sea ice survey of Multi Year pack ice in the Canadian Beafort Sea during the summer of 2011	1
1.1 Introduction	1
1.2 Survey Area	2
1.3 Instrumentation	5
1.4 Regional Data Sampling	6
2.0 GPR and Video-GPS System Data Processing for Melt Pond Detection.....	11
Abstract	11
2.1 System	11
2.2 Additional Equipment and Software	15
2.3 Melt Pond Analysis	16
2.4 Expected GPR Surface Resolution	21
2.5 Melt Pond Plots	22
2.5.1 Plots/Results from GPR Profile527 (from file D2011_228F527.GPR) ...	23
2.5.2 Plots/Results from GPR Profile528 (from file D2011_228F528.GPR) ...	25
2.6 Melt Pond Tables and Statistics	27
2.7 GPR and Laser Brightness	30
2.8 Video Mosaics	33
2.9 Melt Pond Video Analysis	34
2.10 Conclusions and Recommendations	36
2.11 References	36
3.0 EM-Laser Data Analysisfor Melt Pond Identification.....	38
Abstract	38
3.1 Introduction	38
3.2 Instrumentation	39
3.3 EM-Laser Melt Pond Analysis	41
3.4 Conclusions	47
4.0 Conclusions.....	49
5.0 Acknowledgements	50
6.0 References	50

Appendix 1: 2010 Internal BIO Report	51
Laser Brightness Normalization Procedure to Determine Ice Cover Properties in the Gulf of St. Lawrence	51
Abstract	51
Introduction	51
Laser System	52
Field Data	52
Surface Conditions	55
Raw Laser Altimeter Data	59
Normalized Laser Brightness Results	60
Cam-corder Images of Ice and Open Water	61
Conclusions	61
Appendix A - Other Normalized Laser Brightness Plots	62
Appendix B - Cam-corder Visible Light and Near-infrared Images	64

Abstract

Prinsenbergh, S.J., I.K. Peterson, L. Lalumiere and J.S. Holladay, 2014. Identification of melt ponds in 2011 summer Multi-Year pack ice of the Canadian Beaufort Sea with helicopter-borne Laser, Ground-Penetrating Radar and Video. Can. Tech. Rep. Hydrogr. Ocean Sci. 299: vi+65pp.

This report summarises the analysis of identification of melt ponds and estimation of the melt-pond frequency along helicopter flight paths flown over multi-year pack ice of the Canadian Beaufort Sea in the summer of 2011. The data were collected as part of the Imperial Oil Limited (IOL) Ice Cruise 2011, of which the main objective was to conduct on-ice sampling of properties of thick multi-year ice (MYI) floes that represent ice hazards to offshore operations. While on-ice sampling was in progress, regional ice surveys were performed with helicopter-borne sensors to see how representative the specific MYI floes were of the surrounding pack ice. The regional surveys used a helicopter fix-mounted Electromagnetic-laser (HEM) sensor and a Ground-Penetrating-Radar (GPR) during low altitude flight sections, and a Video-Laser system during high altitude return flight sections.

The results from the HEM survey showed that within a large consolidated floe away from the floe edge, no apparent ice thicknesses less than 3m were seen, and yet large bottom-less melt ponds were visually observed and can be identified in video data. Apparently long-period wave mixing was not occurring within the consolidated ice floe, and low-salinity melt water was trapped within the melt ponds. The melt-water could not be distinguished from ice by the HEM system; its return signal is mainly from the saltwater layer found beneath the melt pond. The analysis presented in this report shows how the return brightness of the laser and the GPR return echo strength can be used to identify melt ponds that the HEM sensor cannot distinguish from ice during low-altitude survey flights. The video data collected at high altitude over the same floes on return flights is used to verify the melt-pond frequency inferred from laser brightness and GPR echo strength data. Further field and analysis work is required to narrow the range of estimates of melt pond frequency observed by the three methods.

Résumé

Prinsenbergh, S.J., I.K. Peterson, L. Lalumière and J.S. Holladay, 2014. Identification of melt ponds in 2011 summer Multi-Year pack ice of the Canadian Beaufort Sea with helicopter-borne Laser, Ground-Penetrating Radar and Video. Can. Tech. Rep. Hydrogr. Ocean Sci. 299: vi+65pp.

Le présent rapport résume l'analyse du recensement des étangs de fonte et l'évaluation de leur fréquence le long des trajectoires d'hélicoptère effectuées au-dessus d'une banquise composée de glaces pluri-annuelles, dans la partie canadienne de la mer de Beaufort au cours de l'été 2011. Les données ont été recueillies dans le cadre de la croisière des glaces entreprise par Imperial Oil Limited (IOL) en 2011, et dont le principal objectif consistait à effectuer l'échantillonnage sur place des propriétés des floes composés de glace pluri-annuelle épaisse; ceux-ci représentant des dangers glaciels pour les activités extracôtières. Pendant l'échantillonnage sur le terrain, des relevés régionaux de la glace ont été effectués au moyen de capteurs héliportés, pour calculer la représentativité de floes composés de glace pluri-annuelle distincts, par rapport à la banquise environnante. Les relevés régionaux ont été effectués à l'aide d'un capteur électromagnétique laser et d'un géoradar installés sur un hélicoptère pour les sections couvertes par les vols à basse altitude et d'un système vidéo laser pour les sections couvertes par les vols à haute altitude.

Les résultats du relevé réalisé à l'aide du capteur électromagnétique laser ont révélé que dans un grand floe consolidé, à une distance de son pourtour, aucune épaisseur de la glace de moins de 3 m n'a été observée; cependant de grands étangs de fonte sans fond ont été relevés visuellement et peuvent faire l'objet d'un recensement à partir des données obtenues par vidéo. Apparemment, un mélange de vagues n'a pas lieu dans le floe consolidé, et ce, sur une longue période; des eaux de fonte de faible salinité ont été emprisonnées dans les étangs de fonte. Il était impossible de distinguer les eaux de fonte des glaces dans le système par captage électromagnétique, les signaux de retour provenant principalement de couches d'eau de mer situées au fond des étangs de fonte. L'analyse présentée dans ce rapport démontre comment le retour de la luminosité provenant du laser et la force de l'écho provenant du géoradar peuvent être utilisés pour recenser les étangs de fonte, que le capteur électromagnétique laser ne pouvait distinguer de la glace au cours des relevés effectués à basse altitude. Les données vidéo recueillies à haute altitude en survolant les mêmes floes au cours des vols de retour servent à vérifier la fréquence des étangs de fonte déduite à partir de la luminosité du laser et de la force de l'écho provenant du géoradar. Des travaux sur le terrain et une analyse plus approfondie sont nécessaires pour réduire l'éventail des estimations quant à la fréquence des étangs de fonte observée par les trois méthodes.

1.0 SEA ICE SURVEY OF MULTI YEAR PACK ICE IN THE CANADIAN BEAUFORT SEA DURING THE SUMMER OF 2011

1.1 INTRODUCTION

The ExxonMobil-led Canadian Beaufort Sea ice survey during August 14-24 concentrated on the Multi-Year Ice (MYI) pack ice west of Banks Island (Fig. 1.1). The aim of the survey was to document the properties of ice hazards affecting offshore operation in the Canadian Beaufort Sea. It was the first survey where the Bedford Institute of Oceanography's (BIO's) helicopter-borne sensors were used over predominant MYI to monitor the spatial distribution of pack ice properties. Additional ArcticNet research on specific thick MY ice floes collected physical and chemical sea ice data to document the properties of the thick MYI and to understand the atmosphere-ice-ocean interaction processes in forecasting the impact to climate change on the marine and pack ice environments and ecosystems.

The BIO's helicopter-borne sensors were used to document the ice thickness and ice roughness properties of MYI ice floes sampled in detail by other researchers onboard the Amundsen in addition to the pack ice surrounding the sampled MYI floes. The analysis of the properties of the regional pack ice regions is the main focus of this report with special attention being given to the identification of the spatial distribution of melt ponds within the regional pack ice using data from the existing helicopter-borne sensors.

The report will first discuss briefly ice conditions of the pack ice survey area, then present in two sections the analysis of the identification of melt ponds with data of the GPR and Laser sensors collected along low altitude flight sections for one specific 15 km survey line. The method to normalise the laser brightness for height variations is presented in the Appendix.

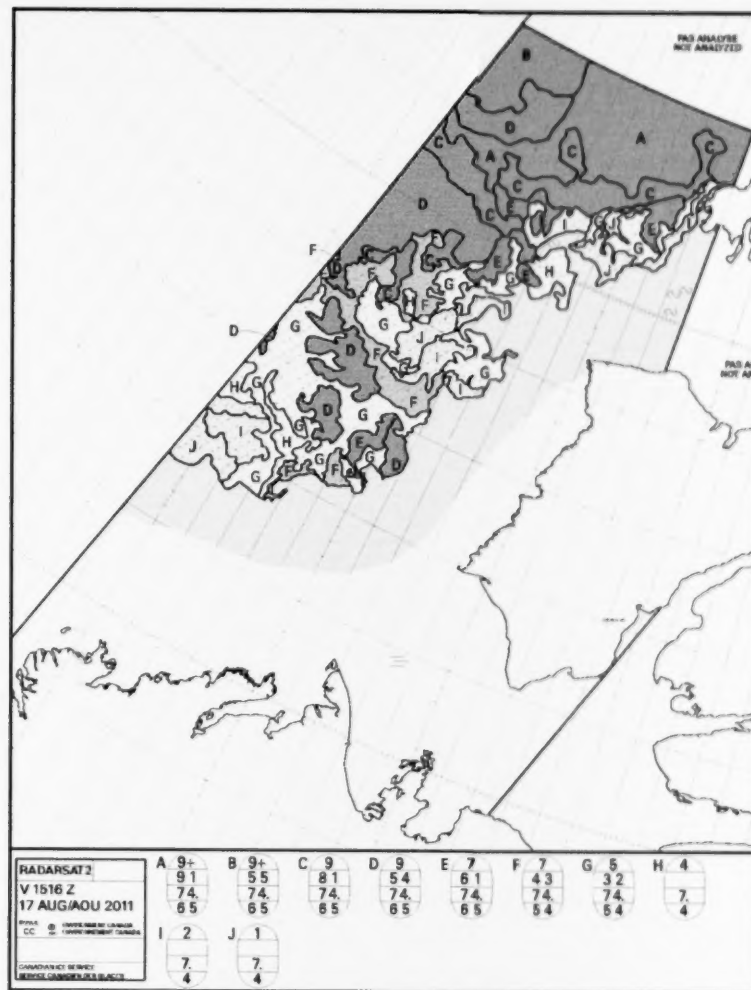


Fig. 1.1 Ice chart of August 17 representing the ice conditions at the start of the ice survey. The survey was done just below the 75°North latitude, the latitude that runs through the middle of into M'Clure Strait and along and into the ice edge.

1.2 SURVEY AREA

As seen from the ice chart (Fig. 1.1), the ice consisted mostly of thick MY ice as the colour variation on the chart indicates mainly the variability in ice concentration rather than a variability of ice type (thickness). A large open water area existed between Banks Island and the main pack ice and the open water condition continued into M'Clure Strait. This open water area was not extensive enough to generate the long period waves as were seen in the summer survey of 2009 that are capable to move into the pack ice and break up the pack ice into smaller floes. A storm, midway through the survey, moved south of the survey area but did not generate the required long period waves to break up the large floes.

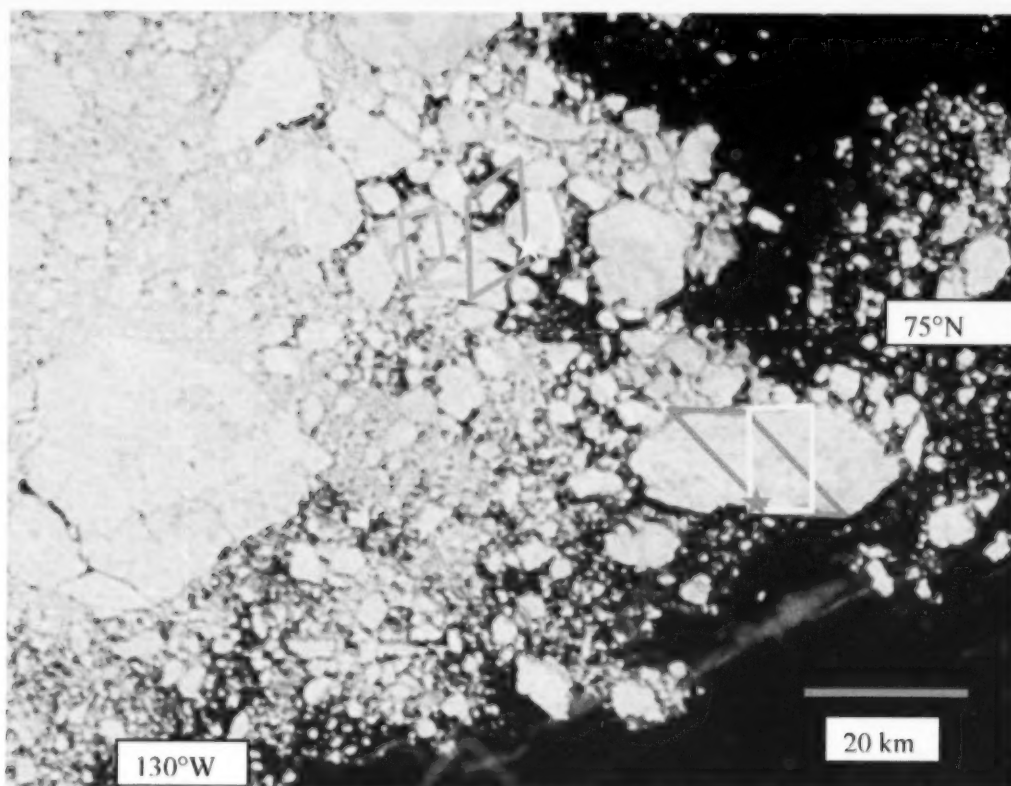


Fig. 1.2 Modis satellite image of August 16 showing the approximate locations of the MY ice sites B1.S1 (red star) and B1.S2 (green star), and the regional areas covered by the ice helicopter survey (coloured boxes).

Figure 1.2 shows the typical ice conditions as seen in a Modis satellite image of August 16 and used to produce ice charts. The B1.S1 floe along which the CCGS Amundsen anchored (red star in Fig. 1.2) consisted of MY ice and appears in the image to be highly consolidated. But as seen in later pictures this large floe contained a lot of melt ponds in various stages of decay that were intermingled with older solid MY pack ice with thicknesses persistently reaching 5-6 m.

The CCGS Amundsen anchored during the survey to two thick MY ice floes so that extensive on-ice sampling by other Amundsen researchers could take place to document their physical and chemical ice properties of the thick MYI for studies of the ocean-ice-atmosphere interaction processes. Extensive sampling with the EM-Laser and Video sensor was done over these two specific MY ice floes to understand how representative the ice conditions of these two sampled MY ice floes were within the regional pack ice. Four regional surveys were done over surrounding pack ice near the icebreaker using 4-6 parallel grid lines each 10-15 km in length along which EM-GPR-Video data was collected. This regional data indicated that ice thicker than 4 m occurred only 20-40 % of the time while ice thinner than 4 m including melt ponds accounted for 60-80 % of the surveyed pack ice. Figures 1.3 and 1.4 shows pictures of the CCGS Amundsen anchored to the two thick MYI floes B1.S1 and B1.S2. The pictures show clearly that the selected

floes were the thickest and largest in the area containing turquoise coloured melt ponds whereas farther away from the icebreaker areas with black coloured melt ponds existed. These black coloured melt ponds were bottomless whereas the smaller turquoise melt ponds mostly found within the thicker ice still contained an ice bottom.

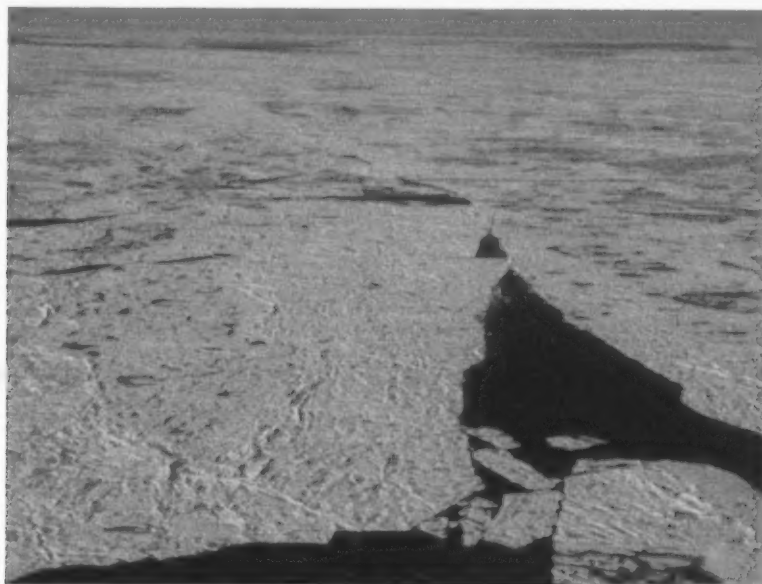


Fig. 1.3 Picture of B1.S1 site with the on-ice instrumented floe left (SW) of the icebreaker and the floe for regional ice distributions on the right.

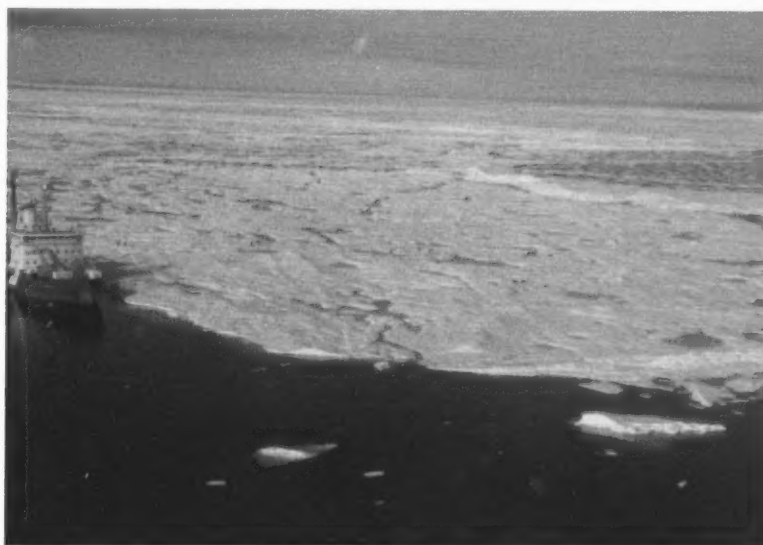


Fig. 1.4 Picture of B1.S2 site with people on the ice right (west) of the icebreaker.

1.3 INSTRUMENTATION

The BO105 helicopter stationed onboard the CCGS Amundsen (Fig. 1.5) was used during the ice survey flights; it was flown by Robert Pelletier and maintained by the helicopter engineer Eddy Perron. The two week-long survey collected ice thickness and ice roughness data with the fix-mounted helicopter-borne Electromagnetic-laser (EM) sensors flown at 5-8 m altitude above the pack ice. A Ground-Penetrating-Radar (GPR) collected data at times simultaneously with the EM sensor. It is designed to measure snow depths, but since limited snow was encountered on the pack ice, less effort was put on the data collection with this sensor. Video and roughness data was collected with a video-laser system flown at 100-120 m altitude along return flight paths covered by the EM system. Details of the sensors capabilities are discussed later in this report.



Fig. 1.5 Canadian Coast Guard BO105 helicopter landing on the after deck of the CCGS Amundsen showing the fix-mounted HEM sensor equipment mounted to the front of the helicopter and the GPR and Video in "Pods" clamped to both sides of the helicopter skid gear.

1.4 REGIONAL DATA SAMPLING

When the data sampling with the helicopter (video and ice thickness) of the site specific MYI floes was completed, ice surveys were done along parallel 10-15 km lines for several regions. The large floe to the North-East of the ice breaker at the site B1.S1 (Figs. 1.2 and 1.3) was sampled and its data is shown below in Figure 1.6. The combined histogram shows that this part of the pack ice consisted of 40 % of ice thicker than 4 m, while the remaining pack ice (60%) included numerous melt pond areas and was less than 4 m thick. As seen in the image (Fig. 1.2), the floe appears to be very compact and the floe B1.S1 where the on-ice sampling was done (Fig. 1.3) was one of the thicker parts of this large floe. However as seen in the picture (Fig. 1.3), other areas of the floe consisted of thinner areas and contained a lot of melt ponds that were actually bottomless.

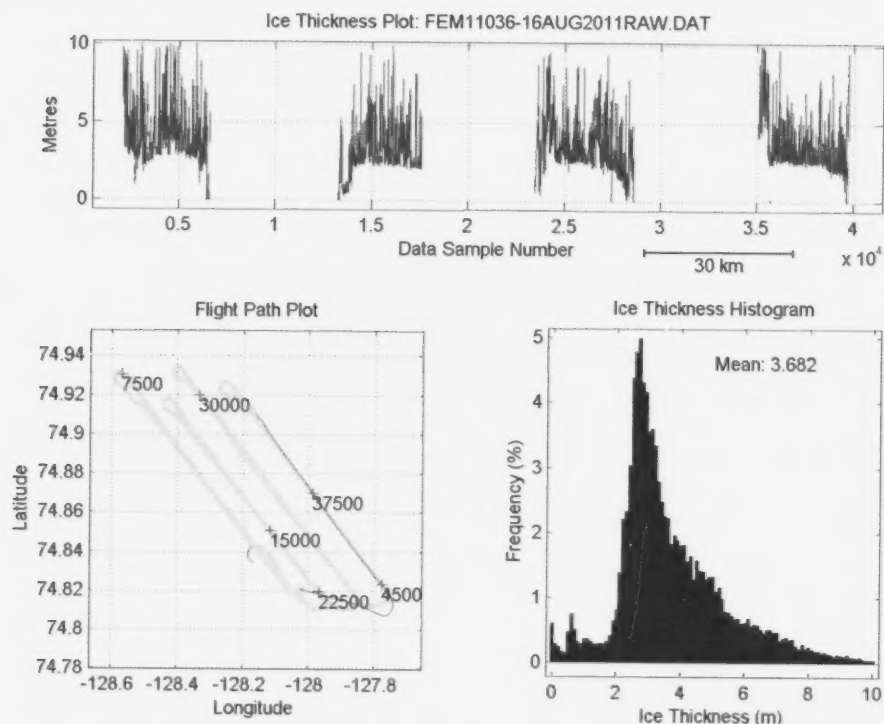


Fig. 1.6 Regional ice thickness survey over the large ice floe northeast of site B1.S1 where the CCGS Amundsen was anchored. The area of the survey is shown by the red box in Fig. 1.2.

Four parallel EM-GPR lines were flown in the NW direction into the light NW winds and four video lines were flown back along the same line at 100m altitude in the SE direction. The floe had a thick ice elongated region along its southern border that may have helped to keep the floe together (Fig. 1.7) and appeared to have stopped any wind waves penetrating the remaining floe to the north. The MY ice away from the melt ponds showed consistently ice thicknesses between 5 and 10 m. The main worry with this data as can be seen in the profile plots of Figure 1.6 is the lack of inferred thin ice away from

the floe ice edge even though large areas within the floe consisted of bottomless melt ponds. The surface layer of fresh water of these melt ponds appear to be protected from vertical mixing generated by long-period wind waves. And without a long open water fetch to the south to generate long period waves by storms, no mixing within the melt ponds appeared to have occurred nor was the floe broken up into smaller floes. The EM data appears to indicate that the melt water within the melt ponds was not well mixed with the under-laying ocean waters. The HEM sensor thus infers these melt ponds as being ice with thicknesses of 2.5 to 3.0 m. This effect disappears at the edges of the floe (Fig. 1.6) where the wave mixing is present and thus thinner ice was observed.

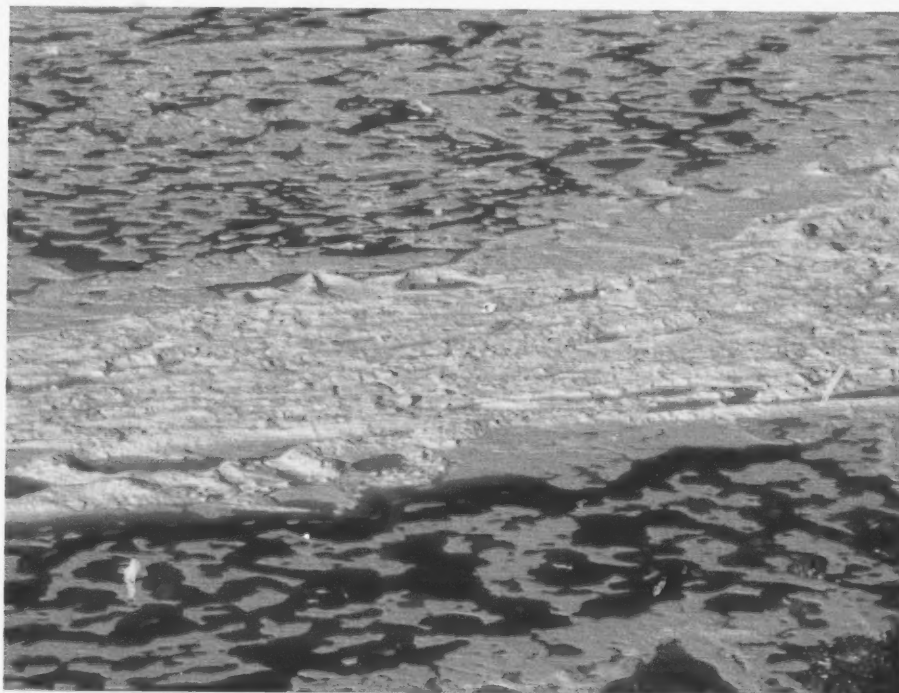


Fig. 1.7 Thick elongated pack ice seen at the start (south) of the long EM ice thickness profiles shown in Figure 1.6.

The video data collected on return flights verifies the presence of melt ponds as seen in mosaics constructed of overlapping video frames (Fig. 1.8). It provides details on the pack ice conditions flown over by the video and is used normally to determine floe and lead distributions. In this analysis the video data is used to calculate what fraction of area is taken up by melt ponds within the pack ice area that was covered by the video mosaic. The short mosaic of Figure 1.8 is from the most north-eastern return flight path of the grid shown in Figure 1.6. The mosaic shows the distribution and presence of melt ponds that typically occurred throughout the regional survey area of the pack ice west of Banks Island flown over by the helicopter. A mixture of melt ponds with and without bottoms appears within the pack ice where apparently vertical mixing of the melt water with the underlying ocean water was limited. Near the edges of the consolidated floes ($\sim 1/2$ km),

wave mixing did appear to mix the melt water into the ocean surface layer as thin ice was inferred by the EM sensor within the ice thickness profiles (Fig. 1.6).

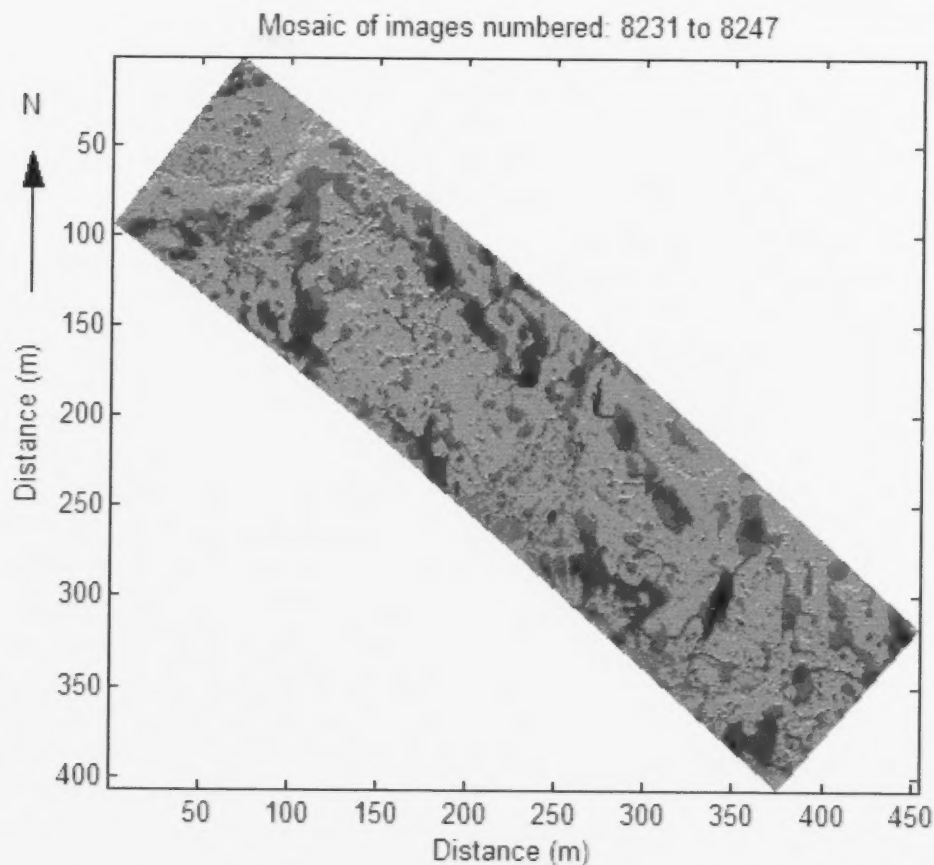


Fig. 1.8 Short mosaic along the return flight of the most North-Eastern flight line of the large MY floe the northeast of floe B1.S1.

After the on-ice surveys were completed, there was time to do regional surveys when favourable weather conditions did occur. Ice thickness plots of three additional regional surveys are shown in Figures 1.9, 1.10 and 1.11. The thickness plots have various degrees of thin ice along the ice thickness profiles which are taken as areas where some wave mixing of the ice melt water of the melt ponds and the underlying ocean layer did occur.

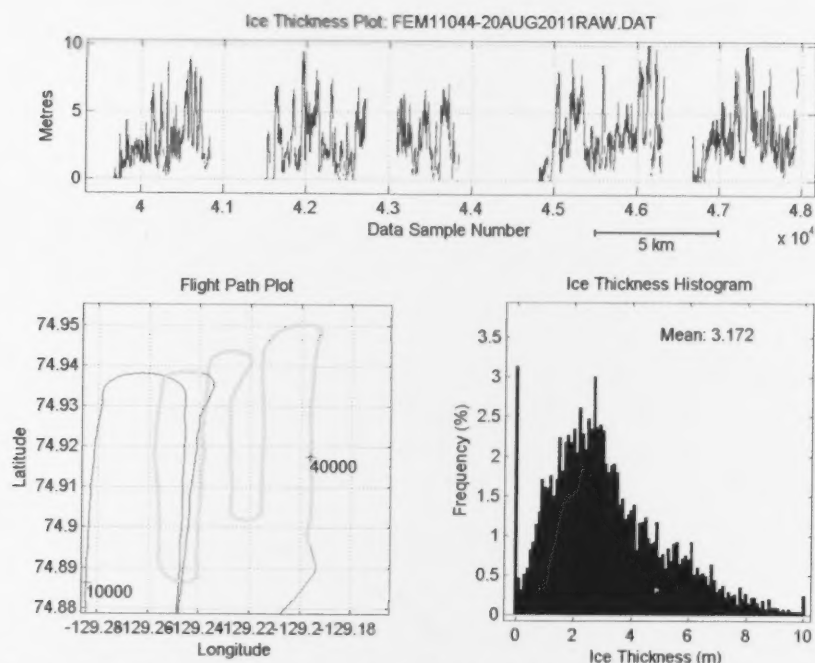


Fig. 1.9 Regional ice thickness survey (FEM 11044) of August 20. Ice thicker than 4 m makes up only 20 % of the area surveyed, yet some ridges do reach 10 m. The area of the survey is shown by the blue box in Fig. 1.2.

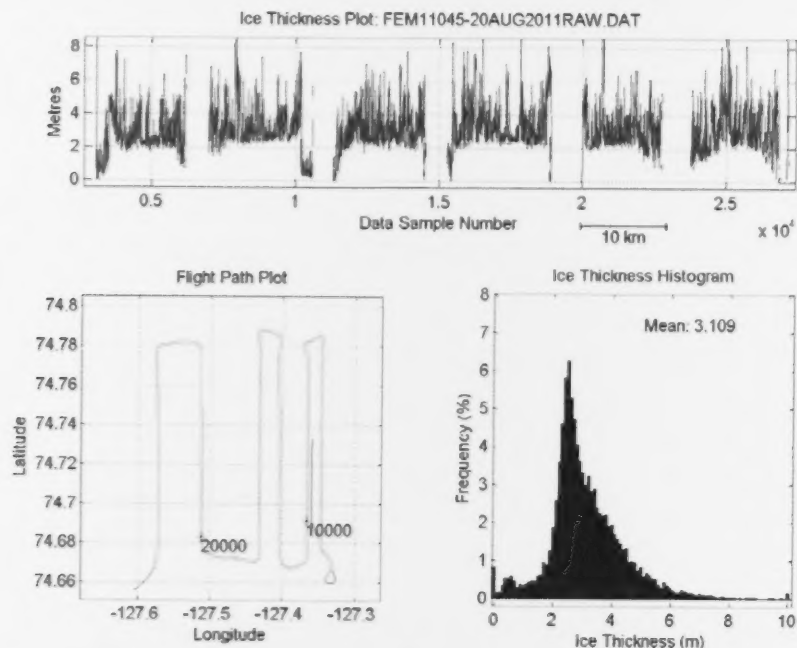


Fig. 1.10 Regional ice thickness survey (FEM11045) of August 20. Ice thicker than 4 m makes up only 20 % of the area surveyed, yet some ridges are up to 10 m thick. The area of the survey is shown by the green box in Fig. 1.2.

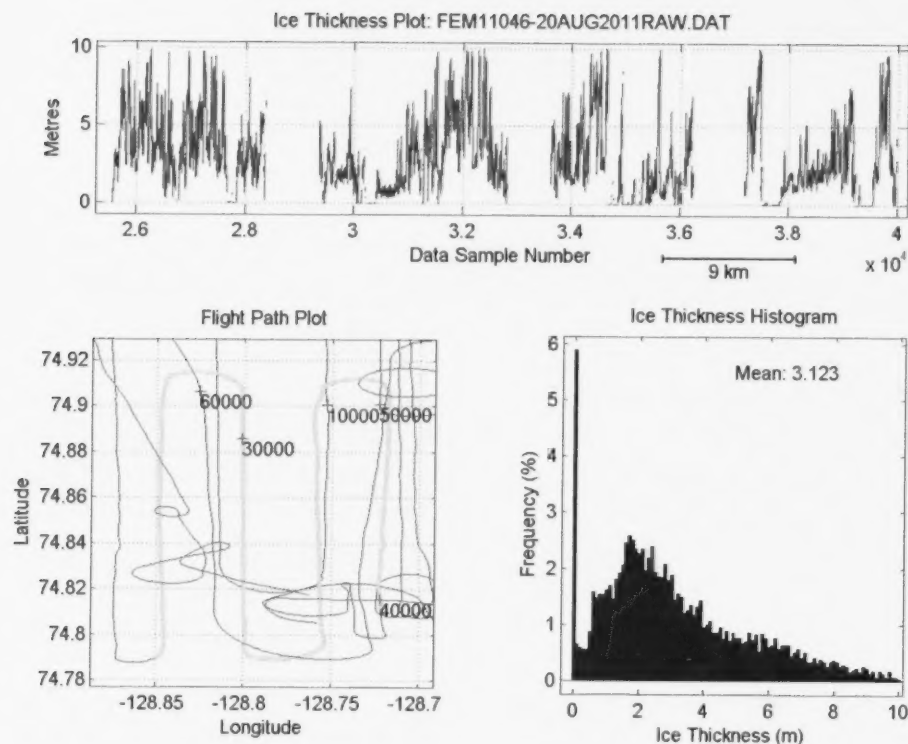


Fig. 1.11 Regional ice thickness survey (FEM11046) of August 20. Ice thicknesses greater than 4 m occurred 40 % over the area surveyed. The area of the survey is shown by the magenta box in Fig. 1.2.

The HEM-Laser system thus provided accurate information on the frequency of thick ice (>4 m) within the decaying summer MYI pack ice; however the frequency of thin ice was obscured by the presence of melt ponds with bottoms as well as bottomless melt ponds where limited vertical mixing of the melt water with the underlying sea water had occurred. Both these melt ponds were inferred by the EM-laser system as sea ice with thicknesses between 2 and 3 m. The large frequency peaks at 2.5-3.0 m in the regional surveys ice histograms (Figs. 1.6, 1.9, 1.10 and 1.11) thus contained a large contribution of the melt ponds and the question and presentation of the rest of this report will concentrate how the return brightness of the laser of the EM-laser system and the strength of the returning GPR echo can be used to estimate the spatial frequency of melt ponds occurring along the low altitude survey lines that contribute to these large peaks at 2.5-3.0 m inferred EM ice thicknesses.

2.0 GPR AND VIDEO-GPS SYSTEM DATA PROCESSING FOR MELT POND DETECTION

by Louis Lalumiere, Sensors by Design, Ltd.

Abstract

This report section documents recent processing work performed using data collected with the BIO helicopter-borne Ground-Penetrating-Radar (GPR) and Video-laser sensors. The topics covered in the report section include first some background information on the Noggin GPR and Video-GPS sensors before presenting plots and tables of the analysis of the GPR data for melt pond detection. Then the results of the analysis of the laser brightness to detect melt ponds is presented and compared to the GPR echo strength results and to the Video data.

2.1 SYSTEM

The Video-GPS Sensor System consists of a helicopter mounting pod, a digital camera, a laser altimeter, a GPS receiver, a laptop-based logging system and a Ground-Penetrating-Radar (GPR) (Lalumiere and Prinsenbergh, 2009). Figure 2.1 shows a photograph of the equipment pod (with the camera and laser altimeter) mounted on the skid gear of a Canadian Coast Guard BO105 helicopter. An additional pod mounted to the skid gear on the other side of the helicopter is used to mount the GPR unit to the helicopter.



Fig. 2.1 Video-GPS Sensor System pod on the BO105 Helicopter.

The Video-GPS System's laser altimeter is a 3-Alpha model by Optech Inc. (Fig. 2.2). It is used to measure flying height and ice roughness, and sampling at a rate of 30 Hz it provides a 1.5 m sample spacing for a flying speed of 90 knots. The laser is 272 mm long, 202 mm wide and 148 mm high and weighs 1500 g. It requires 12 volts to operate and uses 16 watts. The 3-Alpha is configured to output ranges with a resolution of 1mm and provides a laser return brightness value with each range. The Class 1 laser operates in the near-infrared with a wavelength of 905 nm; so the laser brightness values correspond to the near-infrared reflectivity property of the surface being ranged. The beam divergence is 5 mrad (0.28 degrees) and its spot size follows the formula $4 \text{ cm} + (0.005 \times \text{range in cm})$. So at 5 m flying height the spot size is 6.5 cm.

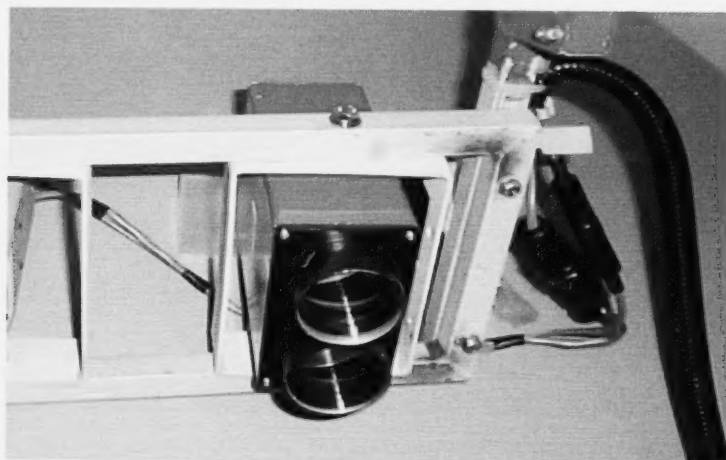


Fig. 2.2 Optech 3-Alpha laser altimeter mounted in the helicopter pod's bracket.

The digital camera used is an Axis 210 by Axis Communications. The Axis 210 camera (shown in Figure 2.3) is 88 mm wide by 157 mm long by 38 mm high and weighs 250 g. The camera is powered using 12 volts with a maximum power draw of 7 watts. An Ethernet link is used to connect the camera to the logging computer. Images are typically collected at a rate of 2 Hz but the rate is determined by the logging system based on the image field of view, flying height and speed.

The imaging sensor in the camera is a 1/4" Sony Wfine progressive scan RGB CCD. Each colour image is 640 by 480 pixels in size and with a typical flying altitude of 120 m each pixel is approximately 40 cm by 40 cm in size. The lens has a fixed 4 mm focal length, an F1.2 aperture and uses the CS mount for attachment to the camera body. The horizontal field of view is 56 degrees and the vertical field of view is 45 degrees.



Fig. 2.3 Axis 210 Network Camera.

The GPS unit used is the Garmin GPS 18x LVC made by Garmin International Inc., Olathe, USA (Fig. 2.4). The Garmin 18X LVC shown in Figure 1.4 is 61 mm in diameter, 20 mm high and weighs only 160 grams. The Garmin model 18X LVC requires a 5 volt supply and runs on approximately 0.5 watts. It outputs data in industry standard NMEA 0183 format over an RS232 serial interface. For the Video-GPS system, the Garmin is configured to output the GGA sentences for latitude, longitude and altitude and the RMC sentence for speed over ground and heading.



Fig. 2.4 The Garmin model 18x LVC GPS receiver.

The GPR system is a Noggin-NIC 1000 from Sensors and Software Inc. of Mississauga, Ontario. A photograph of a Noggin-NIC 1000 is shown in Figure 2.5. The system is 30cm long by 15cm wide and 12cm high and was mounted in a pod which can be attached to the BO105 helicopter's skid gear as shown in Figure 2.1. The Noggin-NIC 1000 requires a 12 volt power supply and requires 8 watts.

The Noggin-NIC 1000 is a unique GPR system which permits operation and control by a computer with no user interaction. This permits the integration of this GPR as an additional sensor into the Video-laser System. The Noggin-NIC 1000 is a very high resolution GPR system, with a center frequency of 1000 MHz and a waveform sampling interval of 0.1 nanoseconds. For this experiment, the device was configured to collect 500

points per scan with 4 internal stacks, which results in a scan rate of approximately 30 scans per second. When flying at 60-80 knots, the ground sample spacing is approximately one sample per 1.0-1.5m. This fine spacing permits the GPR to collect snow features at the same fine scale as the laser for surface ice roughness.



Fig. 2.5 Sensors and Software Noggin 1000 OEM GPR System.

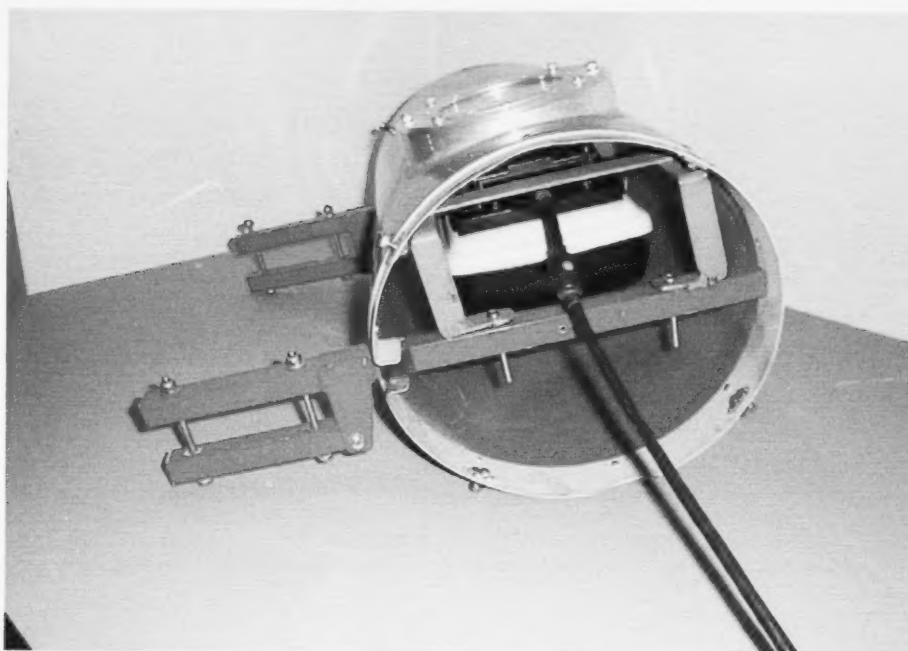


Fig. 2.6 The Noggin 1000 OEM GPR system mounted in the pod.

2.2 ADDITIONAL EQUIPMENT AND SOFTWARE

The logging computer used is a HP/Compaq 8710W laptop computer running Microsoft Windows XP. A graphical user interface (written in Visual Basic) is used to log the sensor data and display the real-time data being recorded such as GPS coordinates and a live view of the video camera image. The data logging software records the data from each sensor asynchronously – applying a time stamp to each sensors data packet as they are received. Under Windows XP, the time stamps are accurate to approximately 10 mS. The post-processing software (Matlab-based Video System Viewer) interpolates and re-samples the time stamps from each sensor onto a common GPS-time base.

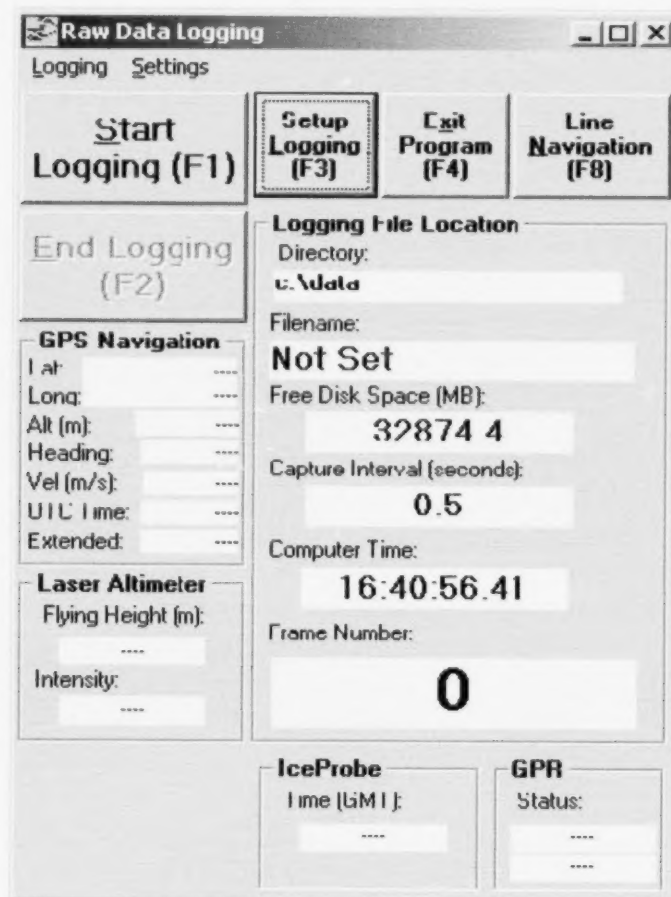


Fig. 2.7 Screen capture of the logging software's main window.

Figure 2.7 shows a screen capture of the logging software's main window. When video logging is enabled, an additional window is provided to show the current camera image.

A distribution box (built by Sensors by Design, Ltd.) is used to connect the laptop data-logger to the sensors and provide the appropriate power supply voltages to each sensor. Vicor brand 28 volt to 12 volt and 28 volt to 5 volt DC-to-DC convertors are used to provide power for each sensor and the data logger – using the helicopter's on-board power supply.

The distribution box has a D-Link brand USB hub to provide a single USB connection to the data logger. As each sensor uses either a serial or Ethernet interface for data transmission, adapters are required to convert the signals to the USB interface. A D-Link brand Ethernet-to-USB adapter is used to connect the Axis 210 Network camera to USB. A second D-Link brand Ethernet-to-USB adapter is used to connect the Noggin. Both the Garmin GPS and the Optech laser have RS-232 serial interface and a serial-to-USB adapter is used with each unit for USB connectivity.

2.3 MELT POND ANALYSIS

GPR data were collected during the August 2011 Beaufort Sea Survey (Prinsenberget al., 2011). While the normal usage for the GPR is to determine snow depths when flying over sea ice, the late summer ice conditions consisted of melting ice with surface melt ponds. These ice conditions opened up a whole new avenue of data processing for the GPR system not previously implemented with this equipment.

The previous GPR processing method described in Lalumiere et al., 2000, uses the time-of-flight of the GPR pulse to determine the depths of the snow layer over sea ice. The GPR is also capable of measuring low salinity ice thicknesses (Lalumiere, 2011). For the melt pond analysis, a match filter-based technique was developed to detect and classify the GPR signal returned from the surface as an open water echo from a melt pond.

From the Wikipedia article on Matched Filters:

http://en.wikipedia.org/wiki/Matched_filter “In telecommunications, a **matched filter** (originally known as a **North filter**[1]) is obtained by correlating a known signal, or template, with an unknown signal to detect the presence of the template in the unknown signal. This is equivalent to convolving the unknown signal with a conjugated time-reversed version of the template.”

Figure 2.8 show a grey scale plot of GPR data from file F528. In this plot, the GPR scans are plotted side-by-side vertically with GPR echoes on the right arriving after the one on the left. In this plot, the absolute value of the signal level is plotted in varying shades of grey with the highest levels plotted as black. The melt pond echoes show up as the dark banding from scan numbers 9206 to 9280 and another pond at 9354 to 9380. The non-dark banded GPR scans are the echoes from areas over pack ice where no water is present. For this plot, the y-axis is given as GPR sample number where each sample represents a sampling interval of 0.1 nS.

To maximize GPR scan rate from the Noggin GPR, the GPR time windows had to be kept as short as possible and as a result the GPR was configured to collect data from the

GPR receiver starting 200 samples after the time when the transmitter fires its pulse. As the GPR sampling time represents the two-way travel time of the GPR pulse and with a sampling interval of 0.1 nS, 200 samples corresponds to 20 nS two-way travel time; this adds 3.015 m to the flying height of any echo seen in the GPR plot (this offset can be seen in the plots shown later in the Melt Pond Section). The melt pond echoes seen in the region centered at scan 9250 arrives at sample number 115 – the two-way travel time from the GPR to the melt pond at this point is $(200+115) \times 0.1 = 31.5$ nS. The flying height over the melt pond at this point is $31.5 \text{ nS} / 2 \times .3 = 4.725$ m (where 0.3 is the rounded-off speed of light in air = .299792308 m/nS).

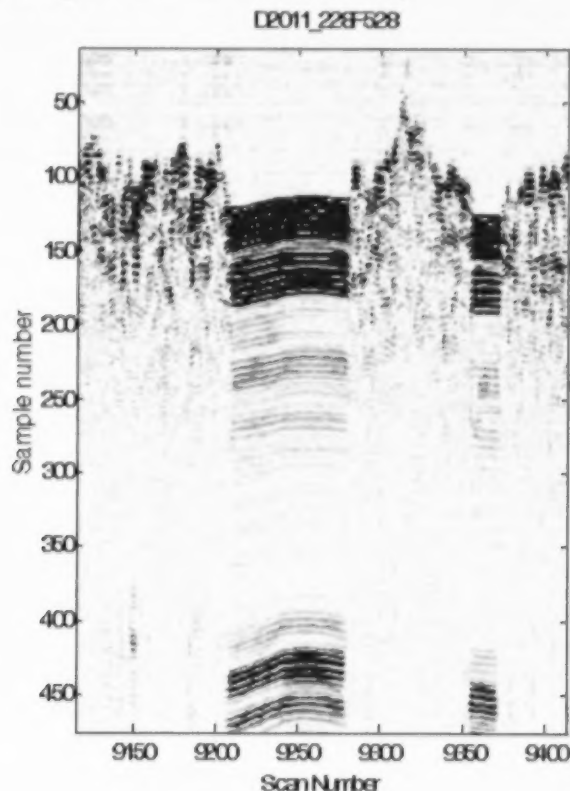


Fig. 2.8 Grey scale plot of a section of GPR data – from file F528.

Figure 2.9 shows the GPR scans from over sea ice and from over a melt pond. The top GPR waveform plotted is scan number 9200 and the lower GPR waveform plotted is scan number 9250 – both are part of the grey scale plot shown in Figure 2.8. Note that the echo from the open water melt pond (in the lower plot – starting at sample number 115) is approximately 10 times higher amplitude than the echo from sea ice (in the upper plot – starting at sample number 65).

The lower plot in Figure 2.9 also shows the multiple reflection echoes. From the study of the GPR plots, there appear to be two multiple reflections – a smaller amplitude start at sample number 390 and a larger amplitude start to arrive slightly later at sample number 415. This can be interpreted as the smaller amplitude multiple reflection coming from the

strong open water return reflecting off the GPR antenna and bouncing down to the ice and back and the larger amplitude multiple bouncing off the bottom of the helicopter cabin.

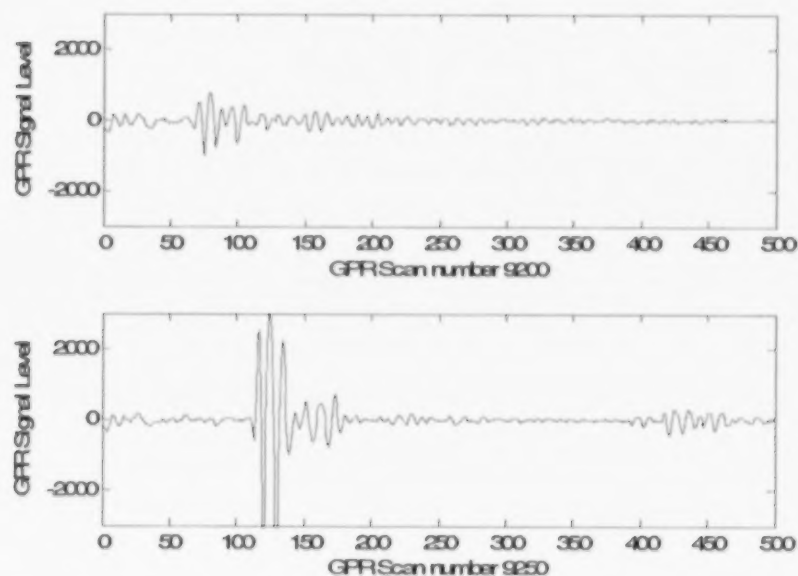


Fig. 2.9 Plot of GPR scans 9200 (sea ice echo) and 9250 (melt pond echo) – to compare with grey scale plot of GPR data given in Figure 2.8.

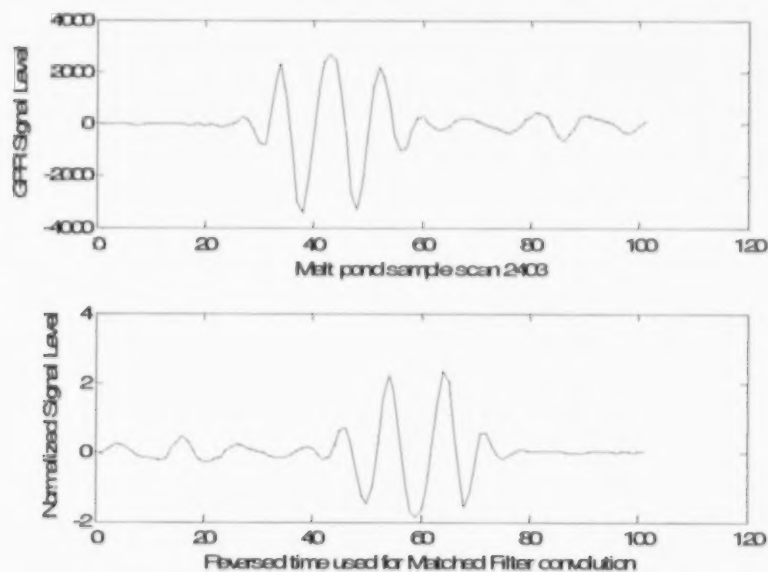


Fig. 2.10 Wave form sample taken from GPR scan 2403 (used for Match Filter) and its reverse time version.

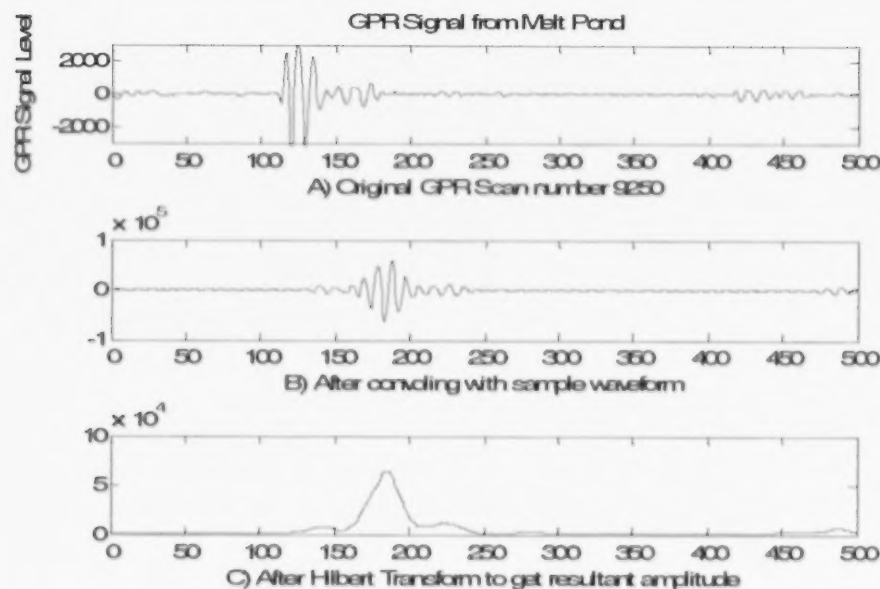


Fig. 2.11 Melt pond result of Match Filter processing. A) shows original GPR scan number 9250 as seen in Figure 2.9. B) shows result after convolving GPR scan with reverse time sample. C) shows amplitude response of B) calculated using the Hilbert Transform.

The added travel path for the second (larger) multiple reflection is approximately 0.375 m – which is similar to the actual distance between the bottom of the GPR antenna and the bottom of the helicopter cabin.

Figure 2.10 shows the waveform sample selected for the Matched Filter and its reverse time version used in the processing. This waveform sample comes from scan 2403 in GPR profile F528 and it was used for all of the Matched Filter processing. In comparison with Figure 2.8, the upper waveform in Figure 2.9 corresponds to the dark banding from the melt pond GPR echoes seen between sample number 100 and 200.

The Matlab function “filter” is used to convolve the reverse time sampled waveform with all the GPR scans for a given data set.

The melt pond result for the Match Filter is shown in Figure 2.11. Plot A) shows the same GPR scan as given in the lower plot of Figure 2.9. Plot B) in Figure 2.11 shows the convolution result as a single pulsed waveform. To detect the Matched Filter result, the signal in B) is rectified using the Hilbert Transform. The Matched Filter “correlation” results are calculated using the absolute value of the Hilbert Transform result and it is plotted C).

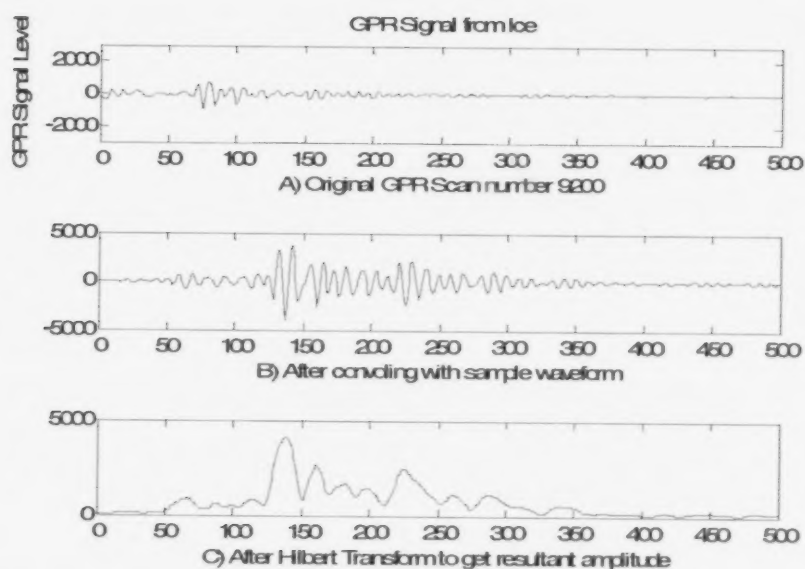


Fig. 2.12 Match Filter processing using GPR scan from ice (not melt pond) A) shows original GPR scan number 9200 as seen in Figure 2.10. B) shows result after convolving GPR scan with reverse time sample. C) shows amplitude response of B) calculated using the Hilbert Transform.

Figure 2.12 shows the Match Filter results from the sea ice GPR return. Plot A) shows the same GPR scan as given in the upper plot of Figure 2.9. Plot B) in Figure 2.11 shows the convolution result; note that there is no short pulse-like result when compared with Plot B) in Figure 2.11. The rectified result shown in Plot C) (using the Hilbert Transform) shows a number of small peaks with the largest being an order of magnitude smaller than the peak seen in Plot C) of Figure 2.11.

The next step in the melt pond processing is to detect the Hilbert transform peak result using a threshold. A threshold value of 50000 was used for GPR line F528. For plotting purposes, the first echo from the surface is located and when plotting, each GPR scan that was detected over a melt pond has an asterisk symbol placed on the GPR plot near the surface echo. To clean up the results, a 3 point median filter is applied to the melt pond plot location.

Several example melt pond plots are shown later in the Plots/Results Section. Figure 2.13 shows an annotated close up view of a section of Figure 2.14 of the Plot Section. GPR scans detected to be over melt ponds have very light red asterisks near the top of the GPR echo from the surface. In this plot, very small melt ponds are circled in red and the larger melt ponds are indicated with the blue arrows. Black arrows are used to locate areas where sea ice is not covered with a melt pond. Multiple reflections are visible in these plots – they are most noticeable when a good reflecting surface provides a strong GPR echo that returns from the surface to be re-reflected off the GPR antenna (or from the

bottom of the helicopter) back towards the surface where the signal is reflected again back towards the GPR antenna. Multiples are easy to detect when the helicopter flying height changes as the slope of the banding from multiple reflection will be twice that of the slope of the banding of the original echo.

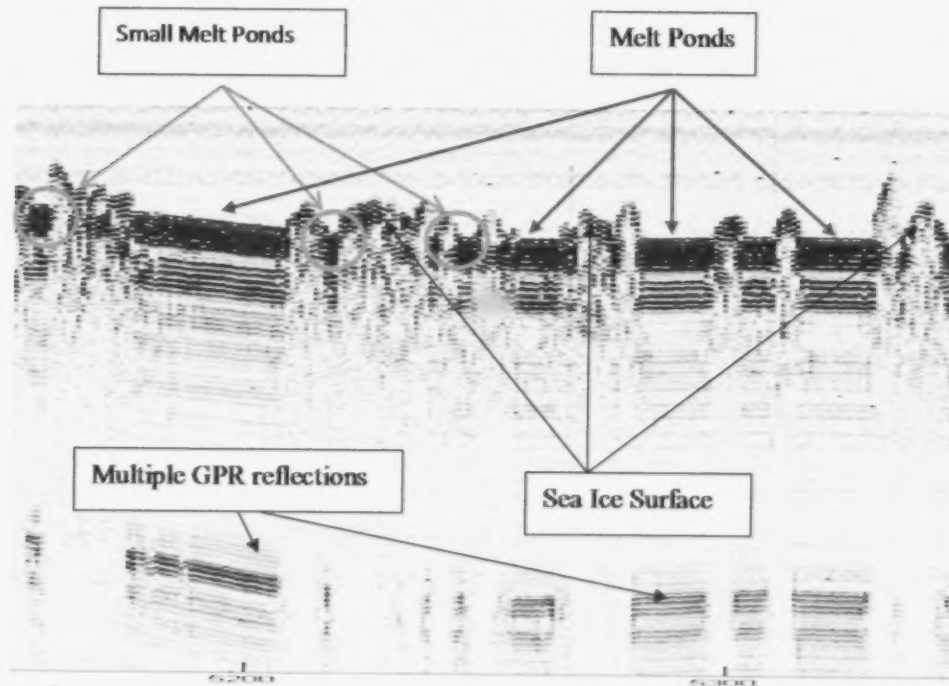


Fig. 2.13 Annotated version of melt pond plot.

2.4 EXPECTED GPR SURFACE RESOLUTION

The GPR footprint diameter is approximately equal to antenna height over the surface. Over a smooth flat reflector, most of the energy is returned from a region with a radius less than one tenth of antenna height (first Fresnel zone). Small GPR targets (in a rubble field) return echoes with much smaller amplitudes than large flat targets (flat ice). When flying at an altitude ranging from 5 to 6 m, a good GPR echo is returned from flat reflectors with size > 50 cm. Also, there will be reflections from corners at the edge of floes and other rubble but they will be small.

Each scan collected in the Noggin is made up from an average of 4 scans, which will tend to average out small echoes from ice rubble.

2.5 MELT POND PLOTS

Two sets of GPR sample plots are shown below. They display the data results of four sub-sections of the two most northeastern lines collected over the regional floe NE of station B1S1. The examples represent locations within the pack ice where a high percentage of melt ponds were seen and thus provide extreme melt pond concentration values. Each data plot covers approximately 700 GPR scans and therefore represents the GPR observations of approximately 1 km of along-track surveyed distance. For these 1 km areas melt ponds concentration values average out to 26 %.

Tables 2.1 and 2.2 show the start and end scan numbers used for each plot. An annotated version of these plots was shown in Figure 2.13 above. For the total of 8 example plots, the y-axis is given as flying height in meters over the surface. The x-axis labels give the GPR scan number plotted – which approximately corresponds to the along-track distance in meters. GPR scans detected to be over melt ponds have a very light red asterisk near the top of the GPR echo from the surface.

Table 2.1 GPR scan number for plots in Section Plots/Results for GPR line F527.

Figure Number	Center Scan	Start Scan	End Scan	melt ponds
2.14	5100	4780	5520	27%
2.15	6200	5880	6600	22%
2.16	7300	7000	7700	24%
2.17	10500	10180	10930	32%

Table 2.2 GPR scan number for plots in Section Plots/Results for GPR line F528.

Figure Number	Center Scan	Start Scan	End Scan	Melt ponds
2.18	5600	5300	6100	23%
2.19	8000	7680	8530	28%
2.20	9400	9100	9840	29%
2.21	14000	13700	14400	23%

These examples are extreme melt pond concentration values of the surveyed floe. As seen in the photographs (Figs. 1.3 and 1.7), no melt ponds were seen at the southern edge of the surveyed floe for 1-2 km or 700 to 1400 scans; and this ridge component of the floe is apparently strong enough to help hold the floe together along with other long ridged areas within the floe. So the overall melt pond concentration of the floe is lower than 26 %.

2.5.1 Plots/Results from GPR Profile F527 (from file D2011_228F527.GPR)

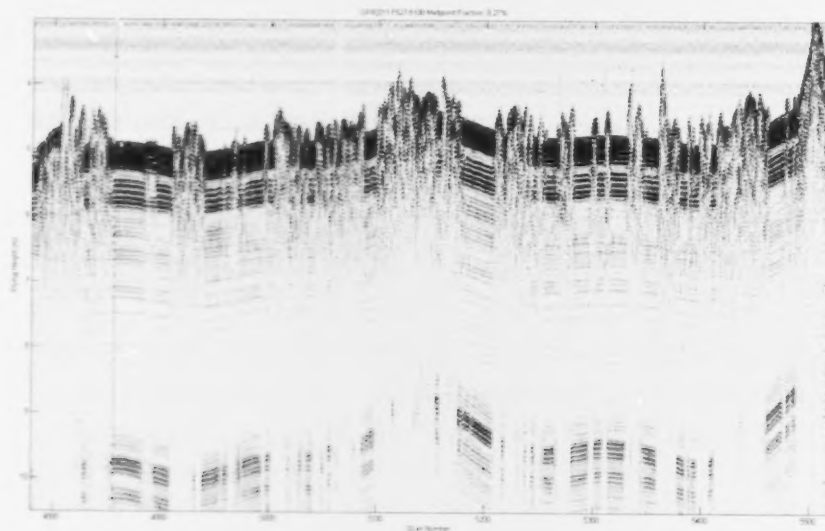


Fig. 2.14 Detected melt ponds for section of F527 centered at scan 5100 - melt pond fraction 27 %.

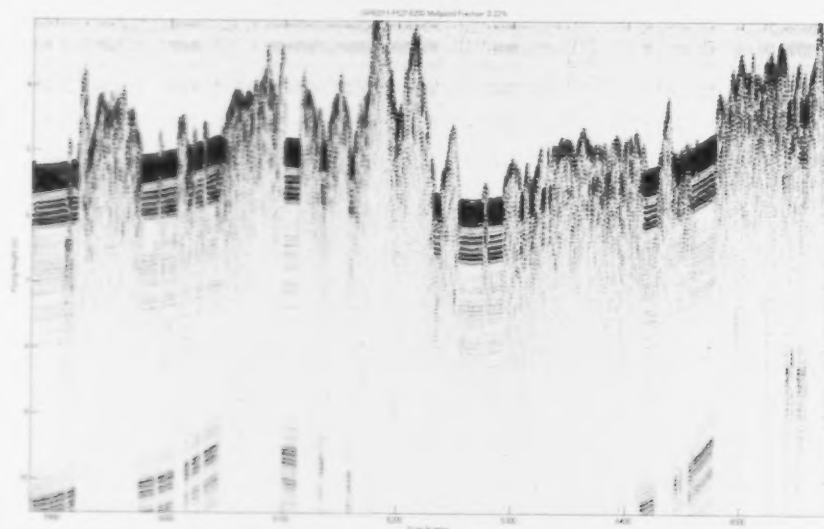


Fig. 2.15 Detected melt ponds for section of F527 centered at scan 6200 - melt pond fraction 22 %.

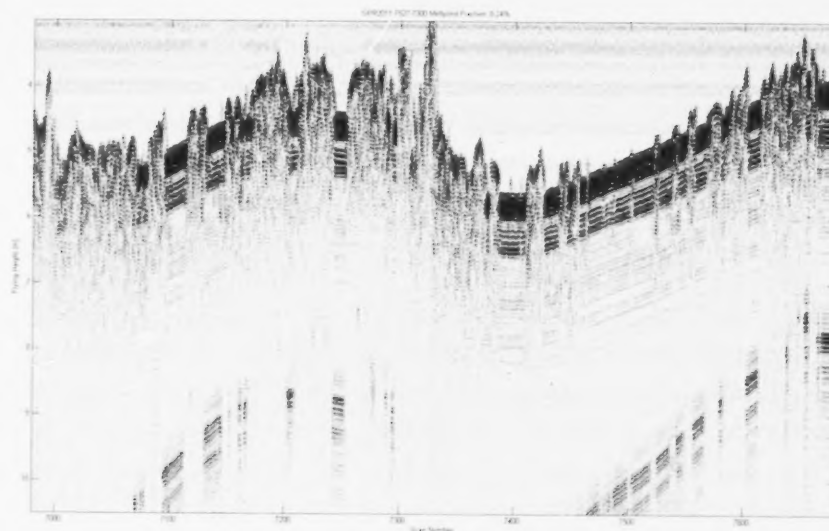


Fig. 2.16 Detected melt ponds for section of F527 centered at scan 7300 - melt pond fraction 24 %.

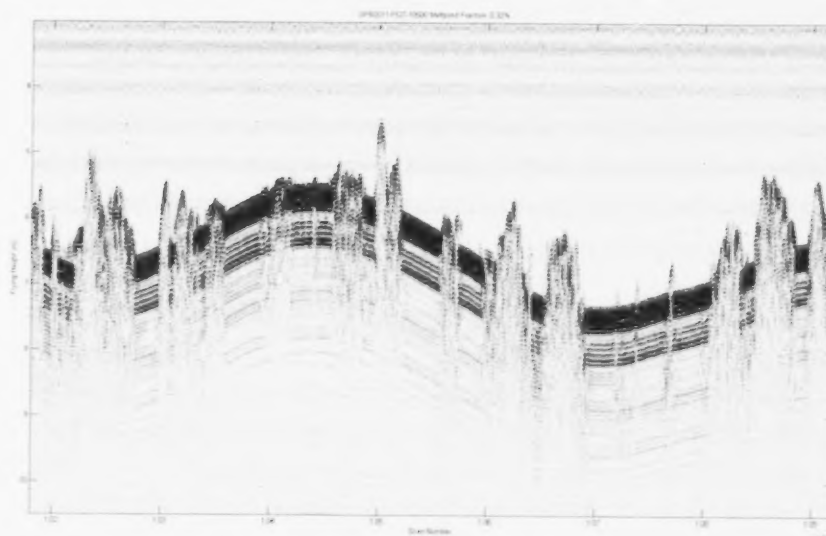


Fig. 2.17 Detected melt ponds for section of F527 centered at scan 10500 - melt pond fraction 32 %.

2.5.2 Plots/Results from GPR Profile F528 (from file D2011_228F528.GPR)

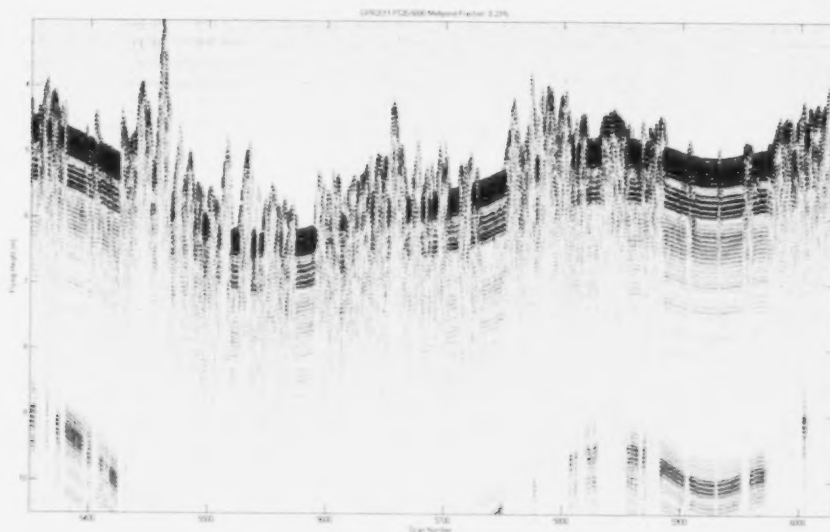


Fig. 2.18 Detected melt ponds for section of F528 centered at scan 5500 - melt pond fraction 23 %.

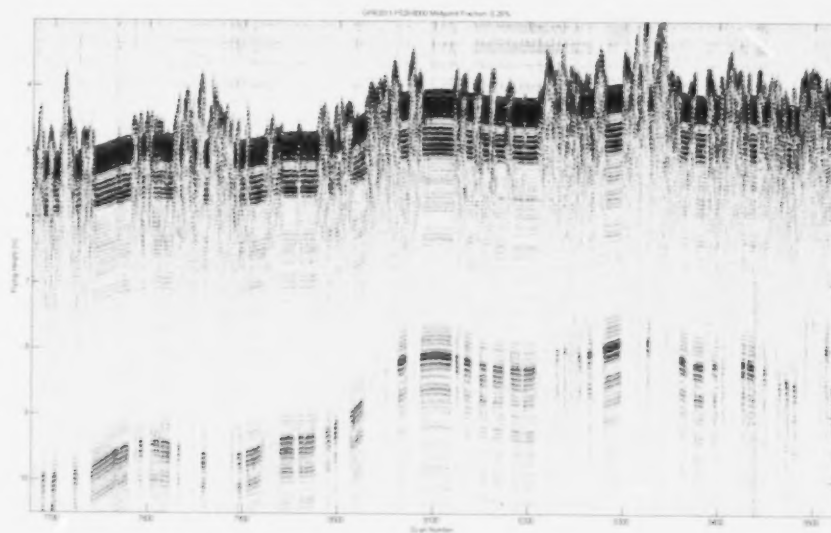


Fig. 2.19 Detected melt ponds for section of F528 centered at scan 8000 - melt pond fraction 28 %.

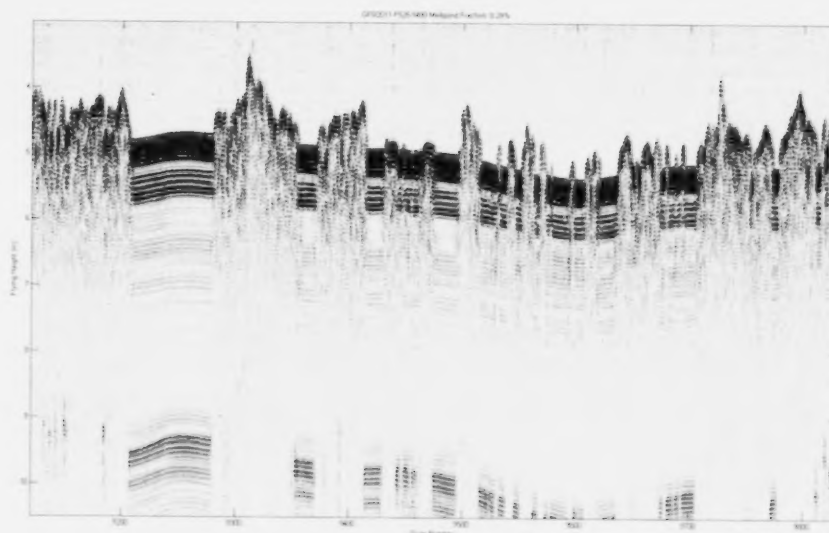


Fig. 2.20 Detected melt ponds for section of F528 centered at scan 9400 - melt pond fraction 29 %.

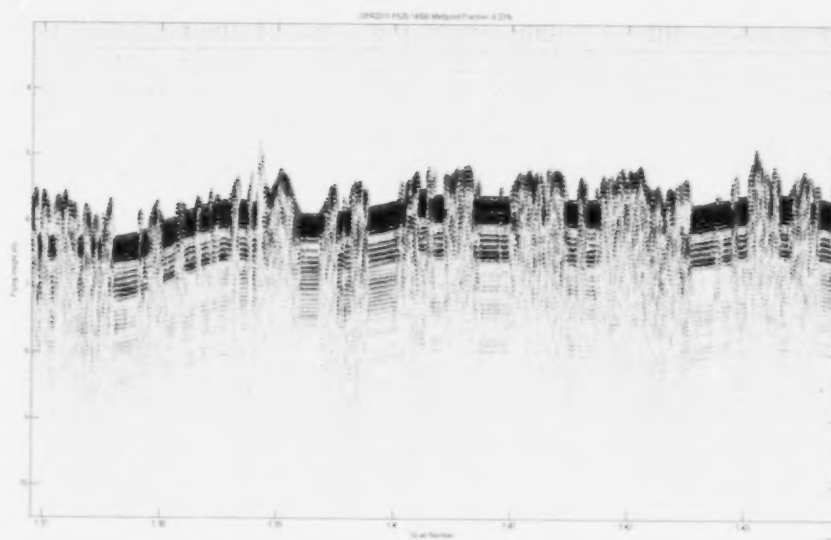


Fig. 2.21 Detected melt ponds for section of F528 centered at scan 14000 - melt pond fraction 23 %.

2.6 MELT POND TABLES AND STATISTICS

Melt Pond Cross Section Length

The above GPR processing classified individual GPR scans as either from a melt pond or not. And these counts can be used directly to estimate the concentration of melt ponds along flight tracks. In order to estimate the cross section lengths of the individual over-flown melt ponds the GPS data can be used and listed as shown below in Tables 2.3.

Table 2.3 GPR detected melt pond results for the section of GPR profile F528 as plotted in Figure 2.20

Start GPR trace #	End GPR trace #	# of traces for the pond	Start UTM Easting coordinate	Start UTM Northing coordinate	End UTM Easting coordinate	End UTM Northing coordinate	Estimated pond cross section length in metres
9151	9151	1	529239.538	8309545.300	529239.538	8309545.300	1.000
9209	9279	71	529191.211	8309584.575	529132.533	8309632.681	75.877
9355	9370	16	529070.775	8309683.920	529058.700	8309693.954	15.700
9416	9429	14	529021.025	8309725.178	529008.892	8309735.199	15.737
9445	9445	1	528996.743	8309745.219	528996.743	8309745.219	1.000
9450	9458	9	528991.768	8309749.317	528984.855	8309755.008	8.954
9476	9495	20	528971.021	8309766.389	528955.241	8309779.358	20.425
9517	9529	13	528936.421	8309794.821	528925.912	8309803.455	13.601
9534	9537	4	528922.595	8309806.180	528919.002	8309809.131	4.649
9548	9550	3	528910.440	8309816.166	528908.784	8309817.526	2.144
9565	9566	2	528896.643	8309827.500	528894.988	8309828.859	2.141
9580	9593	14	528884.513	8309837.462	528872.390	8309847.412	15.683
9599	9606	8	528869.085	8309850.124	528862.200	8309855.771	8.905
9623	9635	13	528848.427	8309867.058	528837.955	8309875.630	13.533
9676	9676	1	528805.381	8309902.242	528805.381	8309902.242	1.000
9683	9685	3	528798.466	8309907.882	528796.529	8309909.461	2.499
9690	9690	1	528793.208	8309912.169	528793.208	8309912.169	1.000
9697	9704	8	528786.285	8309917.810	528781.020	8309922.099	6.790
9774	9776	3	528722.177	8309969.961	528722.177	8309969.961	1.000
9813	9813	1	528690.784	8309995.404	528690.784	8309995.404	1.000
9821	9821	1	528683.835	8310001.020	528683.835	8310001.020	1.000

Table 2.3 shows for one data figure above (Fig. 2.20), a selection of the GPR scans grouped into individual melt ponds over the same range of GPR profile F528. The table provides number of traces of melt pond occurrences identified and the calculated cross section length of each melt pond.

The GPR scans over a melt pond in Table 2.3 were grouped to represent individual melt ponds. The melt ponds are geo-located by getting each melt pond's start and end time as determined from the GPR scans to look up the GPS Latitude and Longitude coordinate. The Latitude and Longitude coordinates are converted to Universal Transverse Mercator projection (UTM) Northings and Eastings, so that the coordinates are in metres. The UTM coordinates can be used to get the length of the melt pond cross section by calculating the Euclidian distance between the start and end points of each melt pond.

Melt Pond Statistics

Using the tables of melt pond start and end coordinates based on GPS locations, statistics on melt pond size for the GPR profiles have been tabulated. The profiles were subdivided into sections 1000 m long (shown in Table 2.4) and 500 m long (shown in Table 2.5). The last line in Tables 2.4 and 2.5 has the total values for each column with the melt pond fraction column showing the average of all the individual segments.

Table 2. 4 Melt pond fraction for each 1000 m segments of GPR profile F528.

Segment Length (m)	Sum of melt pond cross section length in this segment (m)	Melt Pond Fraction in this Segment	Number of melt ponds in this segment
1000	0.000000	0.000000	0
1000	6.431774	0.006432	1
1000	115.771938	0.115772	26
1000	221.896215	0.221896	28
1000	136.139224	0.136139	22
1000	173.657907	0.173658	26
1000	207.960704	0.207961	25
1000	244.407425	0.244407	31
1000	247.623312	0.247623	33
1000	97.548578	0.097549	28
1000	277.638259	0.277638	32
1000	252.983124	0.252983	44
1000	196.169118	0.196169	28
1000	205.816779	0.205817	26
1000	175.801832	0.175802	34
1000	140.427073	0.140427	30
1000	102.908390	0.102908	27
309.79	66.461668	0.214533	11
17309.79	2869	0.16 (average)	452

Table 2.5 Melt pond fraction for each 500 m segments of GPR profile F528

Segment Length (m)	Extent of melt pond cross section length in this segment (m)	Melt Pond Fraction in this Segment	Number of melt ponds in this segment
500	0.000000	0.000000	0
500	0.000000	0.000000	0
500	6.431774	0.012864	0
500	16.079436	0.032159	0
500	10.719624	0.021439	4
500	100.764465	0.201529	21
500	96.476615	0.192953	16
500	125.419600	0.250839	11
500	40.734571	0.081469	8
500	92.188766	0.184378	13
500	87.900916	0.175802	12
500	85.756991	0.171514	13
500	102.908390	0.205817	11
500	105.052314	0.210105	13
500	64.317743	0.128635	10
500	173.657907	0.347316	20
500	99.692502	0.199385	16
500	135.067261	0.270135	16
500	46.094383	0.092189	18
500	41.806533	0.083613	9
500	122.203713	0.244407	16
500	153.290622	0.306581	15
500	101.836427	0.203673	20
500	147.930810	0.295862	23
500	65.389706	0.130779	13
500	120.059788	0.240120	14
500	78.253255	0.156507	10
500	116.843901	0.233688	15
500	113.628013	0.227256	19
500	62.173819	0.124348	14
500	83.613067	0.167226	13
500	56.814007	0.113628	16
500	66.461668	0.132923	16
500	34.302797	0.068606	10
309.79	66.461668	0.214533	11
17309.79	2820	0.16 (average)	436

Using the UTM coordinates for melt ponds found for the various GPR profiles, the along-track Euclidian distance was found. The along track distance was divided into 1000 m

segments or 500 m segments. As shown in Table 2.4 and Table 2.5, each segment has the sum of the melt pond cross section length with that segment, the melt pond fraction for the segment and the number of melt ponds within the segment.

Table 2.4 shows that the average concentration of melt ponds along the total line F528 is 16 %, ranging from 0% to 28 % in each 1000 m segment. In Table 2.5 the same GPR data were split up into 500 m segments, and the melt pond concentration ranges from 0 % to 35 %.

2.7 GPR AND LASER BRIGHTNESS

A brief investigation was performed to determine the usefulness of adding the laser brightness reading for the measurement of the open water fraction and/or floe size distribution. As the laser's wave length is in the near infrared wavelength band, the laser brightness reading might be used to detect when the laser observation is taken from over snow, ice or open water. One problem is that open water sometimes gets no return due to the smoothness of the water ("Laser Mirror effect") and the incident angle, either too much power coming back or no power at all. The Appendix describes in a 2010 internal report how the laser intensity is normalized for height.

The plot shown in Figure 2.22 has a data section of GPR line F527 centered at scan 2300 with the laser brightness plotted below. This plot has been annotated to highlight features in the GPR data that corresponds with changes in the laser brightness. Also, for the following plots, a laser height overlay is placed on the GPR profile plot. One area circled shows the GPR ringing (banding) over a melt pond with high laser brightness. The second area circled shows the GPR ringing over a melt pond with low laser brightness but also no laser altitude values. There is a difference in the banding in the 2 circled areas and that may be due to a difference in the salinity of the melt pond. Some melt pond areas on the left and right of the right red circle do have laser altitude readings with low brightness values.

It is conjectured that the low/high laser brightness is from several things:

- 1) No laser reading was returned
- 2) There is ice under the water layer (melt pond with bottom)
- 3) The dark laser has no ice under the water (bottomless melt pond)

Towards the end of the plots (right hand side) there is a time lag between the laser data and the GPR data.

By visual inspection – there is a slight difference in the GPR response over melt ponds with a bright laser brightness (left circled area) and a dark laser brightness level (right circled area). Future work could implement different Matched Filters – one for a GPR waveform signature from the left circled area and one for a GPR waveform signature from the right circled area. If this GPR ringing difference is due to different salinity levels, it may be possible to detect brackish water in melt ponds – though significant on-ice work would be required to collect salinity-temperature profiles for the validation of this technique.

Figures 2.23 and 2.24 plot the laser brightness on GPR profiles previously shown in Figures 2.14 and 2.15.

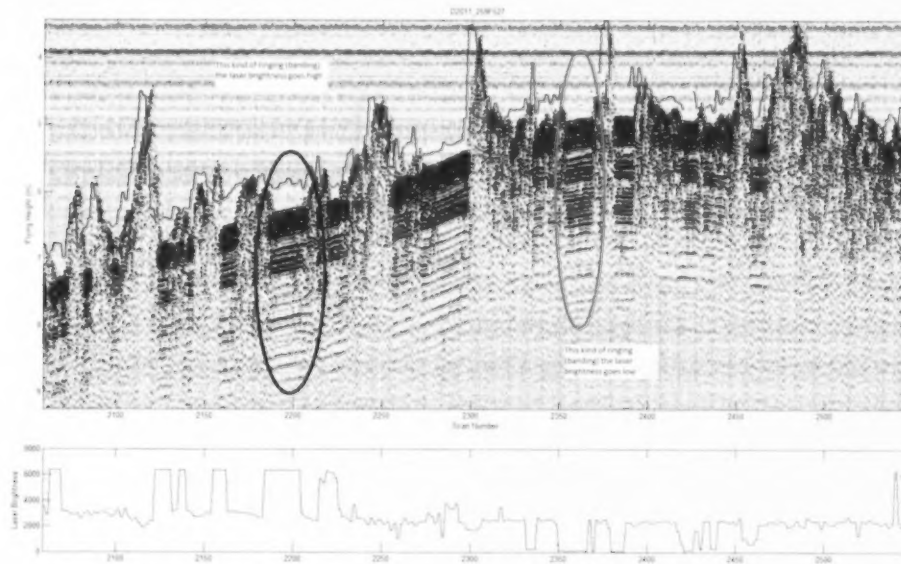


Fig. 2.22 Annotated GPR plot with altitude (top panel) and laser brightness (bottom panel).

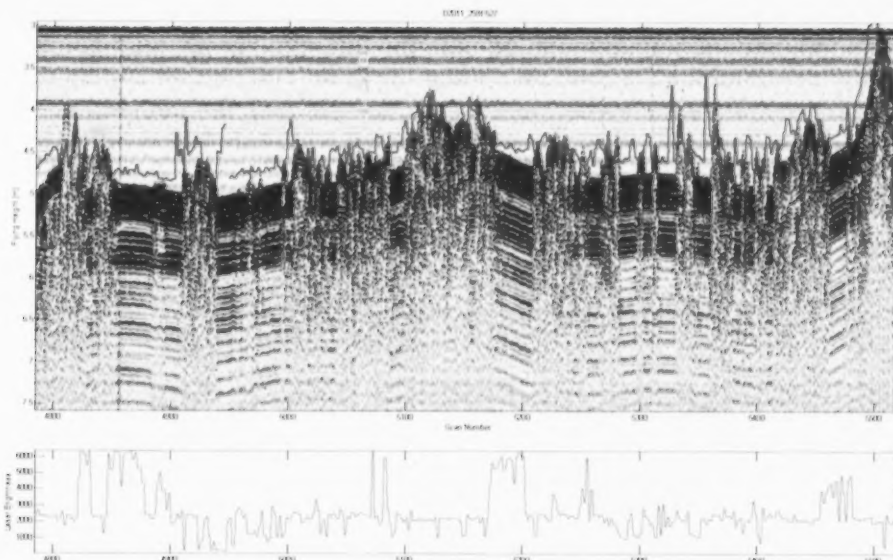


Fig. 2.23 Laser brightness on GPR profiles previously shown in Figure 2.14.

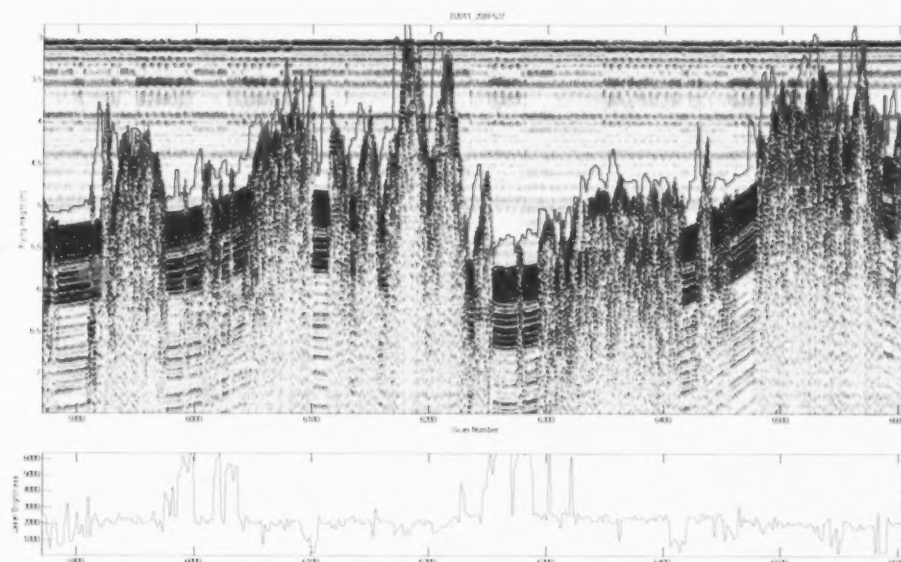


Fig. 2.24 Laser brightness on GPR profiles previously shown in Figure 2.15.

2.8 VIDEO MOSAICS

Video data file F019 was collected flying in a SE direction over the area where GPR profile F528 was collected flying in a NE direction. The geo-located melt pond result for GPR line F528 was plotted over a section of video mosaic created from the images collected in survey F019.

For the complete GPR line F528, the melt pond coordinates do not pass over video images. The melt pond coordinates are off to the east side of the video imagery at the south end; they cross over the video line about mid-point and then are off the west side of the video at the north end. A zoomed-in section of the middle portion was used, selecting a region that lines up with the GPR melt pond Figure 2.20 (F528 centered at scan 9400).

The video mosaic (shown in Fig. 2.25) has the melt pond sections drawn in green with the start GPR scan number. There is an offset of a 95 m east-west and 75 m north-south between the GPR coordinates for the melt ponds and the video image. For this mosaic, the big dark melt pond in the lower right of the video mosaic was used to find the offset of the GPR Melt Pond coordinates to get a rough line up. The alignment starts to drift off at the end of this plot so plotting a longer section of results would not give a good correspondence. The GPR line F528 starts at 246613 seconds and the Video line starts at 247261 seconds, which is approximately 11 minutes later. In an email communication with Dr. Prinsenberg, the ice breaker's GPS indicated a drift speed of up to 1 knot – where 10 minutes would give a drift of 300 metres.

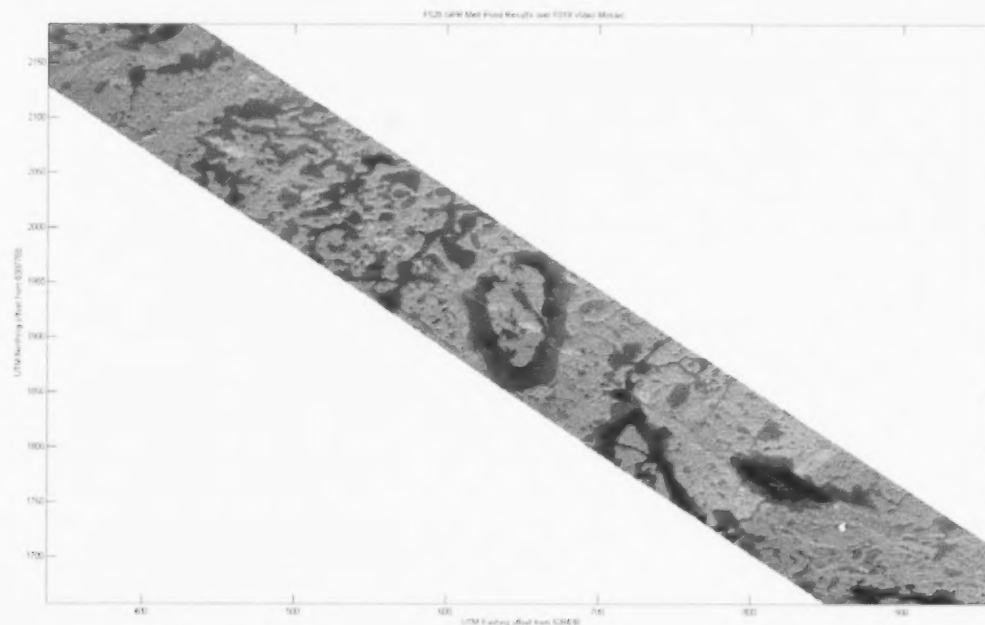


Fig. 2.25 Video mosaic from part of video file F019, with melt pond results from GPR profile F528 (in green).

2.9 MELT POND VIDEO ANALYSIS

For the 1999 Video Sensors System analysis, an image processing technique was developed for automated ice floe size measurement using the video images. This section shows the application of the floe size processing technique being applied to detect and measure melt ponds.

The same series of images as shown in Figure 2.25 were used for this analysis. The Matlab-based Video Viewer's quick-look mosaic was used (with slight modification) to create a linear section of the selected images (as shown in Fig. 2.26). Unlike the geo-referenced mosaic shown in Figure 2.25, the quick-look mosaic plots images together in an along-track sequence using the position difference between each image in the sequence to determine the along-track distance.

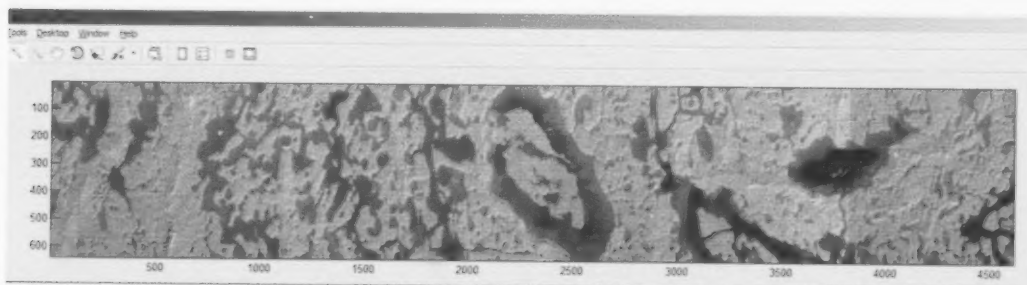


Fig. 2.26 Quick-look mosaic of images selected for the melt pond video analysis.

The Quick-look mosaic was processed by thresh-holding the video grey-level intensity to separate sea ice areas from melt-ponds. This results in a binary (black or white only) mosaic as shown in Figure 2.27. At this point the ratio of total black area (melt ponds) and total area of the mosaic can be calculated to obtain the melt pond fraction. In comparison Figures 2.26 and 2.27, it should be noted that the thresh-holding method of the quick-look mosaic to binary format one underestimate the total melt pond fraction as small melt ponds and narrow leads are ignored as well as the binary melt ponds are all smaller than their original visual ones.

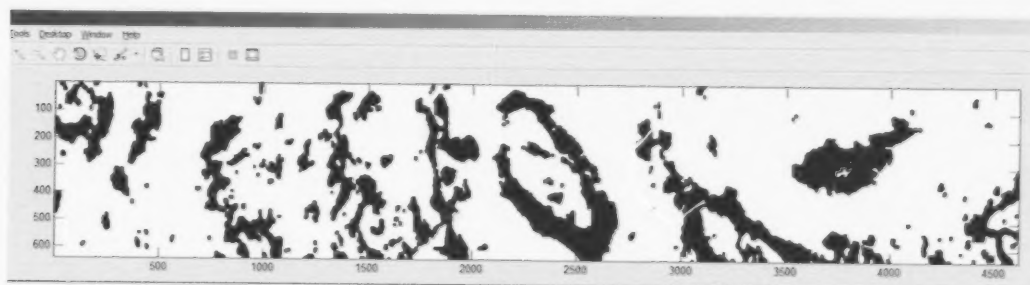


Fig. 2.27 Binary image created by thresh-holding the grey-level mosaic to detect the melt pond areas.

For this mosaic, the ratio between melt-ponds and total area is 0.23. This compares well with a ratio of 0.29 calculated using the GPR melt pond data. The start and end UTM

coordinates from each melt pond found within GPR scan number 9151 to 9821 for GPR profile F528. The length of each melt pond crossing was summed and the ratio between melt-ponds and the total flight path section was calculated.

The binary image was then processed using connected component analysis to get the individual melt ponds. The results from the connected component analysis are shown in Figure 2.28 where each melt pond has a different colour. A histogram of the size of each flow is shown in Figure 2.29.

A Wikipedia article on Connected Components can be found here:
http://en.wikipedia.org/wiki/Connected-component_labeling

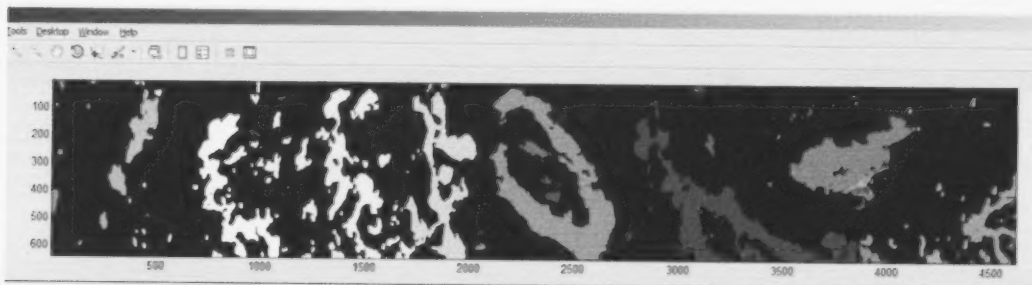


Fig. 2.28 Connected-component-detected melt ponds. Each detected pond is plotted with a different colour.

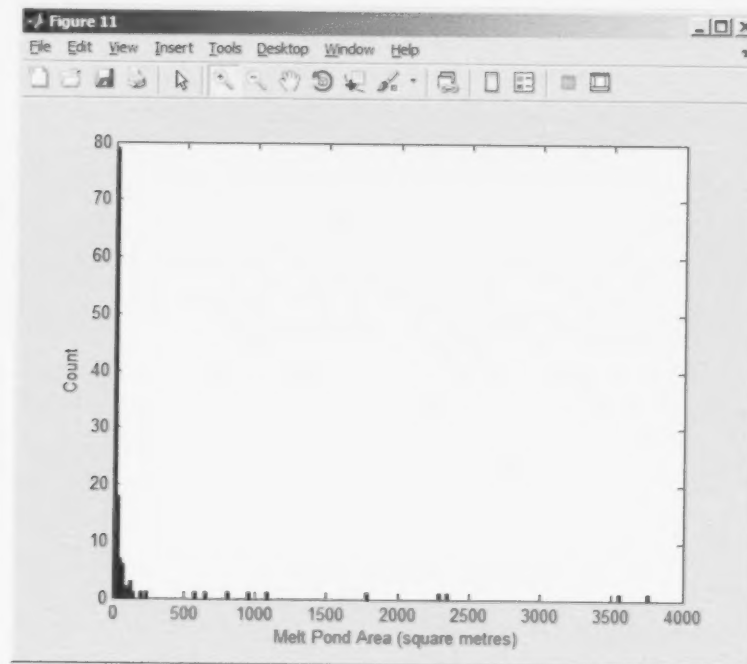


Fig. 2.29 A histogram of the area of each melt pond detected using connected component analysis

2.10 CONCLUSIONS AND RECOMMENDATIONS

The results provided in this report section represent a significant improvement in the integration of the VideoGPS system sensors and the GPR from the state last reported in Lalumiere and Prinsenberg (2009). The use of the GPR data for melt pond analysis provides an additional capability for the GPR beyond its original role for snow depths over sea ice. This is particularly useful for the GPR as in late summer ice conditions provide melt ponds while any snow would be too wet for successful GPR snow depth measurements. Using the number of scans that identify melt ponds versus the total number of scans of the track's profile provide the best and simplest way to obtain the concentration of melt ponds (but not their size distribution) along the flight track.

The video image processing results are visually appealing, but due to ice drift and rotation there is difficulty aligning the 50 to 100 m high altitude video data collection flights accurately with the 5 to 6 m high GPR data collection flights. There may be hundreds of metres of ice drift if the survey flights are separated by 10 minutes. Both GPR brightness and video methods however do provide an estimation of the melt pond occurrence within the pack ice for a specific region although one being derived from a narrow line data file while the other covers a swath width of over 50m. The video analysis method needs more work to avoid underestimating the melt pond concentration by ignoring small melt ponds and narrow leads.

Some very large video mosaics were produced during the development work for the results shown in Section 2.8. When originally developed (Lalumiere, 1999), this was not possible due to computer memory limitations. A mosaic created using all the images in a video survey at full resolution may be hundreds of megabytes in size. With the recent availability of a 64-bit version of Matlab, it may be useful to add the full mosaic feature to the Video Viewer as computer speed and memory no longer limit the mosaic creation.

The Matlab processing developed for this work consists of scripts that are manually adjusted for each data file and GPR profile segment. Further work could be done to automate the various processing steps and provide menu options in the Matlab-based Video Sensor System Viewer to perform the newly developed processing.

As seen in Figures 2.21, 2.22 and 2.23, the laser altitude data plotted over the GPR data does not line up properly. Also, there appears to be a problem with the time stamping of the laser data after long periods of data collection. Some debugging of the helicopter-based data acquisition software is required to fix this problem.

2.11 REFERENCES

Lalumiere, L., S. Prinsenberg and I. Peterson, 2000. Observing Pack Ice Properties with a Helicopter-Borne-Laser-GPS Sensor. In Proceedings of the Tenth (2000) International Offshore and Polar Engineering Conference, Seattle, USA, May 28-June 2, 2000, Vol. I, pp.697-703.

Lalumiere, L. and S. Prinsenber, 2009. Integration of a Helicopter-Based Ground Penetrating Radar (GPR) with a Laser, Video and GPS System. In Proceedings of the Nineteenth (2009) International Offshore and Polar Engineering Conference Osaka, Japan, June 21-26, 2009, Vol. I, pp. 658-665.

Lalumiere, L. 2011. GPR Capabilities for Ice Thickness sampling of Low Salinity Ice and for Detecting Oil-In-Ice. Can. Contractor Rep. of Hydrography and Ocean Sciences #56, iv+36.

Lalumiere, L.A. 1999. Video Sensor System Analysis Report. Can. Contract. Rep. Hydrogr. Ocean Sci. 55: ix + 71 p.

Prinsenber, S.J., Ingrid Peterson and Scott Holladay, 2011. IOL Helicopter Survey Report 2011, Survey period August 11-25. Internal report for the Bedford Institute of Oceanography, 21pp.

3.0 EM-LASER DATA ANALYSIS FOR MELT POND IDENTIFICATION

Scott Holladay, Geosensors Inc.

Abstract

Electromagnetic Induction (EM) systems have provided pack ice thickness and roughness measurements from the Canadian ice-infested coastal waters since the early 1990's. Their laser data is primarily used to provide the height of the EM-Laser system above the ice cover required, and along with the estimated height above the ocean surface provided by the EM data is used to estimate snow-plus-ice thicknesses along helicopter flight tracks. The laser data is also used independently to determine the surface roughness of the ice cover.

In this report section another use for the laser data is being investigated and that is to see if its brightness can distinguish the locations of melt ponds and leads within the pack ice. The analysis will show that indeed the laser brightness can be used to estimate the frequency of melt ponds along flight tracks for the Multi-Year-Ice (MYI) surveyed in the summer of 2011 in the Canadian Beaufort Sea. The results are compared to results obtained by the data analysis of the Ground-Penetrating-Radar and Video presented in the previous section 2.

3.1 INTRODUCTION

Towed or fix-mounted helicopter-borne Electromagnetic (HEM) Induction systems operated since the early 1990's by personnel of the Bedford Institute of Oceanography (BIO) have provided snap shots of sea ice thickness distributions over a large areas limited only by the helicopter range (200 km) from fuel stations. The measurements are important for safe and efficient navigation by ships in ice-infested waters, and are provided either directly to offshore operators or indirectly as input to ice charts produced by agencies such as the Canadian Ice Service. Ice thickness measurements are also used to narrow pack ice data ranges stated in regulation codes for operating in Canadian ice-infested waters. In addition, ice thickness measurements are used in scientific research for studying atmosphere-ocean interaction processes, for assessing changes in pack ice condition due to climate change, and as input and verification data for atmosphere-ice-ocean coupled forecast models.

3.2 INSTRUMENTATION

HEM systems contain one or more sets of transmitter and receiver coils. The transmitter coil produces a primary magnetic field that induces eddy currents in nearby conductors. In sea-ice covered regions, the major conductor is seawater, which has a conductivity of ~ 2.5 S/m that is about two orders higher in magnitude as the conductivity of sea ice. The eddy currents in turn produce a secondary magnetic field that is sensed by the receiver coils. In essence, the amplitude and phase of the secondary field relative to the primary field is used to measure the distance of HEM sensor to the ice-seawater interface. The laser altimeter mounted in the system is used to measure the distance to the surface of the ice (or snow if present); and the difference between the two distances gives the ice-plus-snow thickness (hereafter referred to as ice thickness).

In the 1990's, towed HEM ice-measurement systems (birds) were used by BIO personnel, with the first system being funded through Transport Canada that had frequencies of 2.5 and 100 kHz and a bird length of about 4 m. The system was used between 1991 and 1995 in the Canadian Arctic, near St. Anthony, Newfoundland, in the southern Gulf of St. Lawrence and near Cartwright, Labrador. A second towed HEM system, or "Ice Probe" was built in 1995 and used annually until the late 1990's in the Gulf of St. Lawrence and in 1996 over the Labrador Shelf. The second towed system consisted of a 4.2 m long bird and used 30, 90 and 150 kHz frequencies. However, the 150 kHz data was not used because of high noise to signal ratio in the data associated with this frequency. The EM footprint size was 38-75 m for a sensor surveying height of 10-20 m. The Ice Probe contained an accurate laser altimeter, and a GPS-based orientation sensor to measure bird pitch and roll. Gravity-based orientation sensors such as used in the first towed HEM system are less accurate because of their data sensitivity to accelerations in the bird. A small computer console strapped in the back seat of the helicopter performs the real-time data inversion, logs the data, and controls the operation of the sensor by means of an operator control box from the front passenger seat of the helicopter. The console outputs ice thickness and ice conductivity data at a rate of 10 Hz, corresponding to a sampling interval of 3.5 m for a flying speed of 80 mph. Correction for EM drift is done by obtaining periodically (every ~ 10 minutes) background measurements at high altitudes (> 130 m). Video data was collected at the same time as the helicopter was at an altitude of 50m providing a narrow video window width of 50m.

In the late 1990's, a HEM system fix-mounted on the nose of a helicopter was developed through funds of the Canadian Coast Guard (CCG). It is less cumbersome for the pilots to operate fixed-mounted systems from CCG icebreakers than towed systems (Fig. 2.1 in the GPR section). With the introduction of the fix-mounted HEM system (often referred to as the IcePic or PIC), the logistics of collecting the data was greatly simplified, the footprint size was reduced as one could fly the sensor nearer to the pack ice surface thereby reducing the EM footprint and providing more accurate measurements of level ice thickness when soft-landing to collect spot samples.

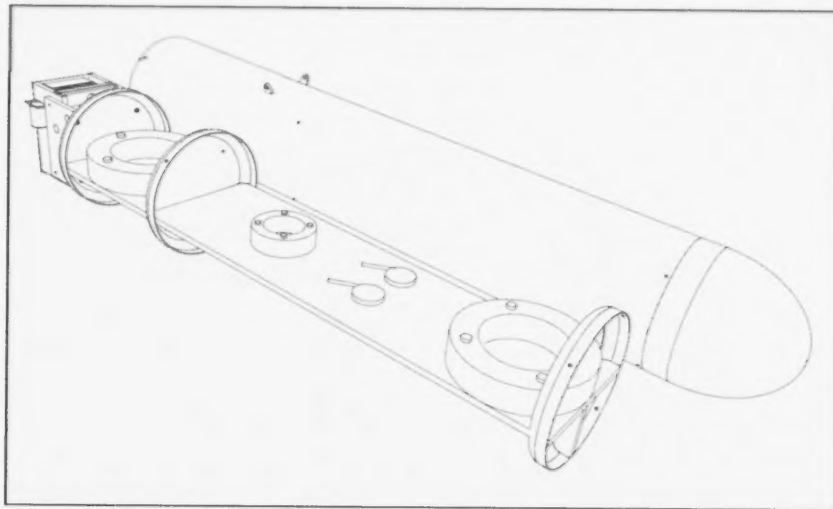


Fig. 3.1 The PIC sensor system schematic next to its mounting tube showing the receiving coils and GPS sensors on the flat platform and the electronics and transmitting coil and electronics at the end connecting to the helicopter (left).

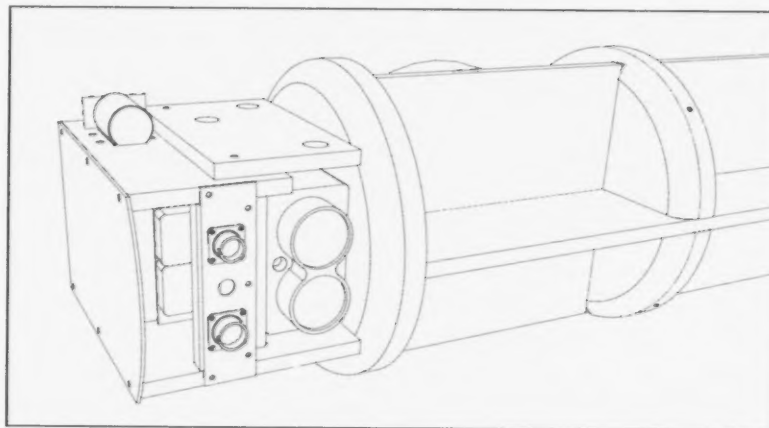


Fig. 3.2 Bottom schematic view of the electronics showing the laser lenses and connecting plugs for cables going to power and control systems inside the helicopter.

Figure 3.1 shows the PIC sensors on its platform alongside its mounting tube with the two receiving coils and two GPS sensors on the platform extending as far away from the helicopter. The transmitting coil is near the end of the platform and along with the electronic controls and laser is located at the far end (left) of the sensor platform that connects to the helicopter (Fig. 3.2). An opening in the mounting tube allows unlimited view of the laser and access to the connecting plugs for cables that transmit power to the EM-Laser-GPS sensors and digital data from the sensors to the PC console strapped in the back seat of the helicopter.

The fix-mounted HEM system, called "Ice Pic", was originally intended to obtain spot samples of level ice thickness by soft-landing the helicopter on the ice and averaging the incoming 10Hz data for several seconds. During soft-landing, the helicopter's skids but not the helicopter's weight are placed on the ice. It was also found that ice profiles could be obtained by flying at low altitude (up to 6m) over the ice. The fix-mounted HEM system operates at frequencies of 1.7, 5.0, 11.7, and 35.1 kHz, and has a coil separation of 1.2 m. Like the Ice Probe, it provides ice-plus-snow thickness, ice conductivity, and laser height data at a sampling rate of 10 Hz. The sensor height above the pack ice surface is 1.1 m with the helicopter skids on the pack ice surface. Thus for 1m ice, the EM footprint ranges from 6 m for spot sampling on the ice surface, to 18 m for profiling at low flying altitudes. The system's small console on the back seat of the helicopter logs the data and controls the operation of the sensor by means of an operator control box.

3.3 EM-LASER MELT POND ANALYSIS

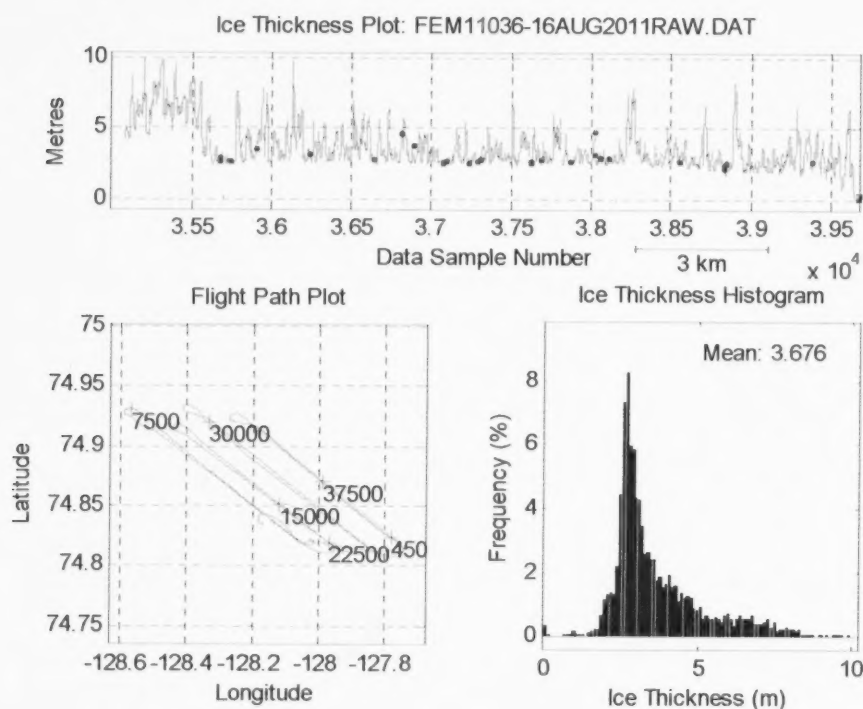


Fig. 3.3 Fourth and last ice thickness profile sampled over floe NE of MYI on-ice station BIS1. Profile is about 15 km long and since the data is sampled to about every 3.5 m, about 4500 samples are collected for survey flying speed of 80 mph. Dots within the profile indicate weaker laser or EM signals and thus uncertain data point locations.

As done for the GPR analysis, the EM-Laser analysis for melt pond identification will concentrate on the EM and Laser data sets collected over the MYI floe northeast of the station BIS1 and in particular the last line within the EM data file FEM11036 that

crosses the MYI floe as both GPR and Video data analysis is available for comparison. It is the most north-eastern line in Figure 1.6 and shown above in Figure 3.3. When ice thickness data is being collected, laser data of the HEM system is available and this data availability would make this sensor in particular the most useful sensor to see if its brightness data can be used to identify the distribution of melt ponds along flight tracks. In contrast, the GPR data is not always available and video data is collected normally on return tracks and thus not simultaneously collected with the EM ice thickness data as its spatial coverage at low altitude is too limited.

In addition the laser brightness data is directly linked in time to the ice thickness so that if a melt pond is identified one knows the ice thickness around the melt pond and when found to be thicker, the melt pond most likely has a bottom and has no drainage connection to the ocean. Whereas if the ice around the melt pond has the same thickness as the melt pond depth, the melt pond is most likely bottomless.

The 15 km long ice thickness profile (Fig 3.3) shows a thick MY ice section of the floe at the start of the line; a picture of this thick ice was shown in a photograph in the Section 1 (Fig. 1.7). Not all of the MY ice of this narrow strip of thick ice was sampled as the helicopter did not reach surveying height in time. The thick MY ice ridge is one of several thick ice ridges that appeared to have held the large (15km x 12km) floe together and this southern particular thick ice region protects the floe from breaking up into smaller floes by any wind waves approaching the floe from the south. It also appears to stop the wind waves penetrating the floe, minimizing the vertical mixing of the melt water in ponds with ocean water in the bottom-less melt ponds. As can be seen in the picture (Fig. 1.7), just behind the 1.0 km wide MY ice section (passed over in 25 sec) is a large area of thin ice and melt ponds that provides a good contrast in ice properties and melt pond distributions relative to the thick MY ice region at the edge of the floe. The "minimum" ice thickness which we are taking to be the depths of the unmixed freshwater melt ponds is 2.7 m at the start of the profile and slowly shallows towards the end of the line where mean depths of 2.0 m occur. Some thinner ice regions with 1.5 m thick ice are present at the end of the profile line where a small lead was present marking the end of the floe.

In the top panel of Figure 3.4 the ice thickness, laser height and laser brightness data are shown for a 2.5 km subsection from the start of the long profile shown in Figure 3.3. It covers the thick MY ice ridge section and shows ice thicknesses of 6 to 10 m (dark blue line) while flying at a survey altitude of 6 to 8 m (light blue line). With a mean ice thickness of 8 m and a sensor altitude of 7 m, the EM sensor distance to the ocean surface layer is 15 m giving an EM footprint (averaging diameter of the ice thickness data) of 45 m. This means that the average 10m thick feature is at least 45 m wide and does represent major ice hazard to marine shipping. The light green line in the top panel is the laser brightness and shows only a few spots where the laser brightness decreases, and is taken to represent possible positions of melt ponds. Even within the areas where large ice thicknesses occur, small melt ponds are present as seen in the picture (Fig. 1.7). These melt ponds have ice bottoms and contain fresh melt-water which along with the rest of the ice below the melt ponds is interpreted by the EM sensor being all sea ice. For this

small MY thick ice subsection, the melt ponds according to the laser brightness occurred 9 % along the linear flight patch where laser brightness data was available.

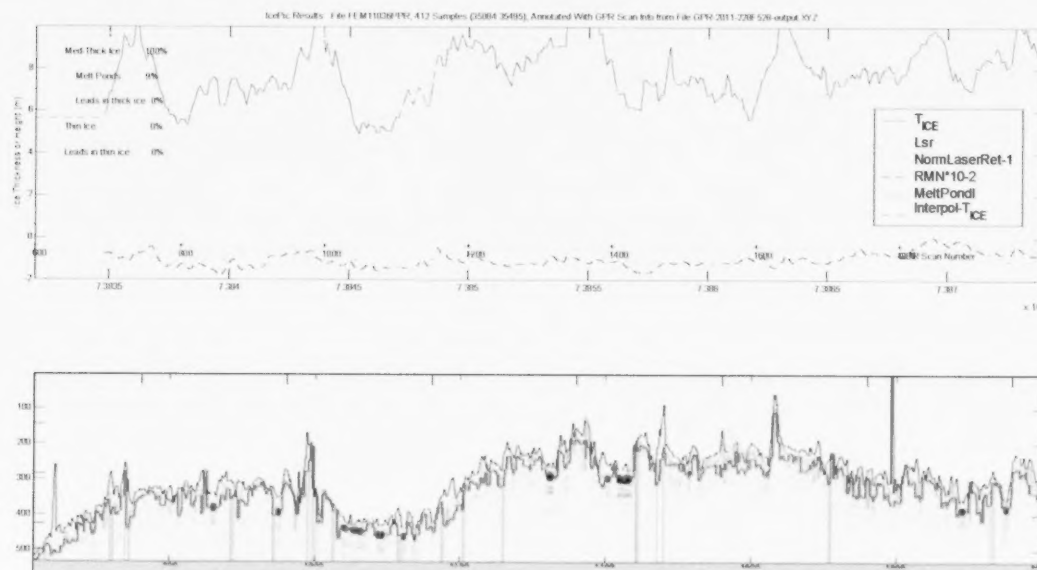


Fig. 3.4 EM-Laser (top panel) and GPR (bottom panel) profile data of a 2.5 km flight section of the thick MYI ice at the start of the ice profile shown profile in Figure 3.3.

The analysis of the individual sample point data of Fig. 3.4 indicates that melt ponds occurred 9 % along its profile length somewhat higher than visually is indicated by the summation of length of red dots and red lines; but this is probably due to the non-100 % availability of laser data. The same is true for Fig. 3.5 where the analysis found melt ponds through sample points occurred 37 % along the shown profile, while visually the red dots/bars make up about 30 % of the profile length.

The bottom panel of Figure 3.4 displays the realigned GPR data collected at the same time as the EM data and shown in the top panel. Most of the melt ponds identified in the GPR profile by the dark echos align well with the locations where the EM laser brightness plot shows a decrease in amplitude (positions underlined in red). There is no perfect one-to-one correspondence in identification of melt pond locations between the EM's laser and GPR data as at some locations the GPR data shows possible locations of melt ponds while the EM laser appears to have trouble obtaining brightness values. This may be caused by the "Laser Mirror effect", when the laser reflection over flat, still water becomes a narrow beam and at times is not reflected back to the laser sensor's receiver, and thus no laser and laser brightness is available. So the GPR profile plot indicate visually that melt ponds may occur more frequently along this flight section than the 9 % indicated by the Laser; however the GPR applies a three point filter and actually has lower values (0-4 %) for the 2.5 km start of this line (Table 2.5 in section 2) as most of the small melt ponds and melt pond edges are ignored.

Adjacent to this thick ice region at the start of the survey line, the EM sensor monitored an area of thin 2.5 m ice before again monitoring a 5 to 8 m thick ice region. This EM-laser profile data along with the GPR data is shown in Figure 3.5. Although melt pond locations are identified in both the thick and thin ice, those in the thicker ice normally consists of single data points and thus represent small melt ponds of the order of the data sampling interval (~3.5 m). Larger melt ponds are seen where thinner ice is present and here little ice sail peaks above the water surface can be seen. In photographs such as (Fig. 1.7) it can be seen that within these areas bottomless melt ponds existed within a field of thin decayed pack ice. The laser brightness data analysis indicated the occurrence of melt ponds along the line section was 37 %. In contrast the GPR analysis (Table 2.5) indicated that melt ponds could be identified in this region (four 392 m sections) at a frequency rate between 11 % and 29 %, a lower rate than indicated here by the EM's laser sensor. The sampling rate of the GPR is 3 times faster than the EM laser having a sample interval of 1 m versus 3.5 m of the EM's laser; but the GPR data uses a 3-point median filter to the melt point location data and that thus may underestimate the total frequency rate by eliminating the small melt ponds and edges of the melt ponds, even though the laser may underestimate the melt pond frequency also because of missing data due to the "Laser Mirror effect".

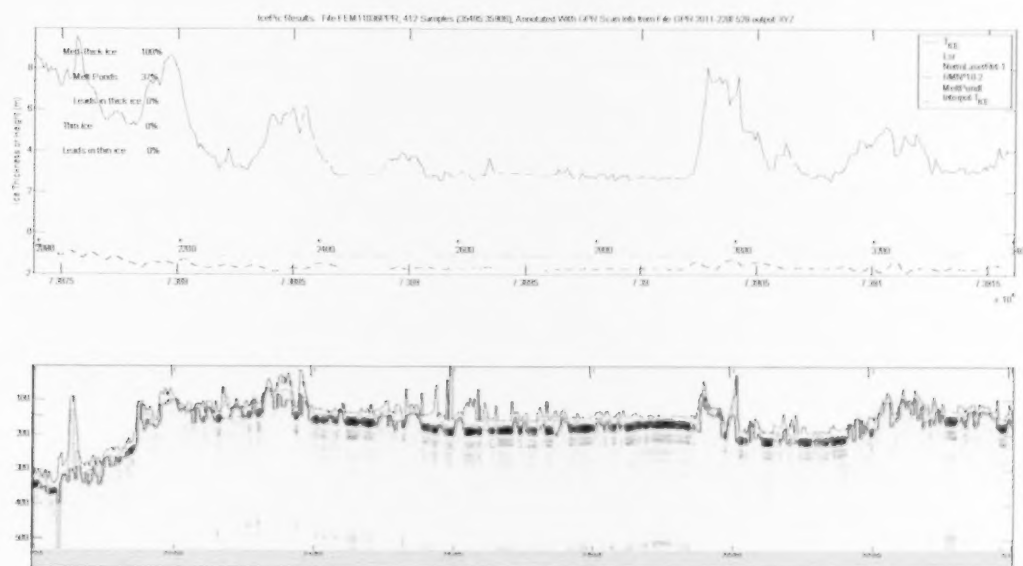


Fig. 3.5 EM-Laser (top panel) and GPR (bottom panel) profile data of a 2.5 km line section adjacent to the section of Figure 3.4 showing numerous melt ponds in thin ice.

The results of the laser brightness analysis for the start of the EM-GPR profile line are re-shown as a normalized laser brightness histogram (Fig. 3.6) where the y-axis shows the frequency of occurrences of laser data samples binned into brightness intervals that are plotted along the x-axis. The total histogram has 866 laser brightness samples and thus

covers a track length of 4 km for sample interval of 3.5 m. As shown in Figure 3.6, the normalised laser brightness does separate nicely the data into two distinguishable peaks. One represents the melt ponds and one the pack ice itself.

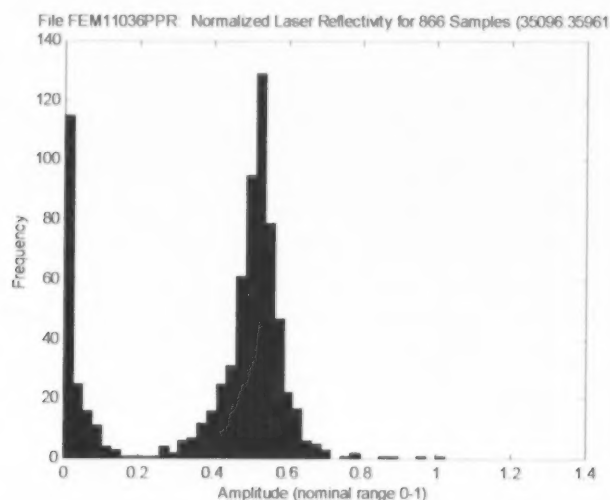


Fig. 3.6 Normalized laser reflectivity data covering the start of the fourth profile line shown in Figure 3.3 and representing part of the two data sections shown in Figures 3.4 and 3.5. The melt pond frequency represented by the low laser brightness samples account for ~20 % of the data.

Three more examples of EM laser brightness data along with the realigned GPR data are shown for the same long survey line in Figures 3.7, 3.8 and 3.9. These are further examples of pack ice regions along this survey line where a high population of melt ponds did exist with surface layer of ice and freshwater existed in an 2 to 3 m thick layer.

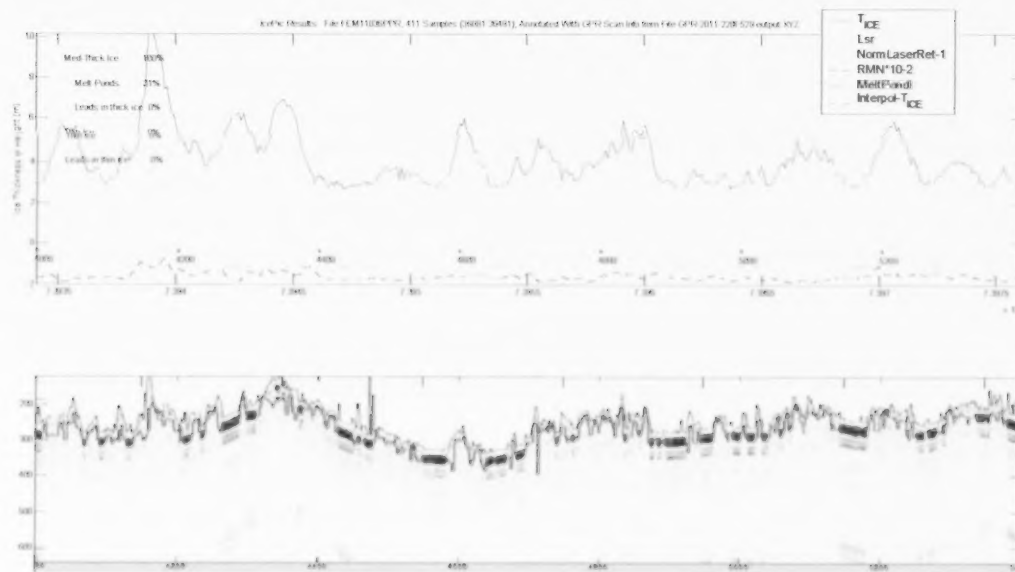


Fig. 3.7 EM-Laser (top panel) and GPR (bottom panel) profile data of a 2.5 km line section adjacent to the section of Figure 3.5 showing numerous melt ponds in thin ice.

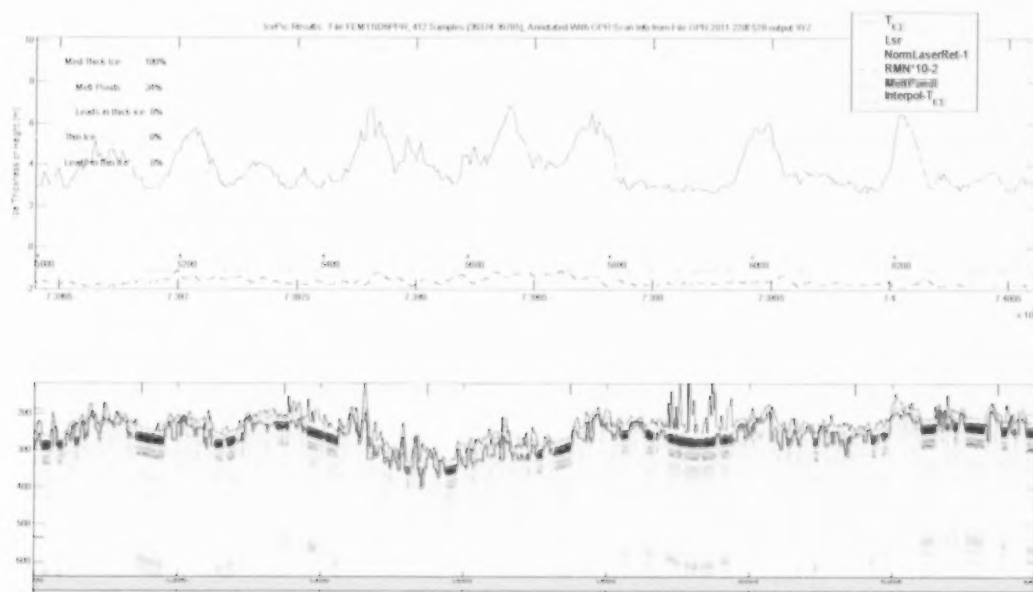


Fig. 3.8 EM-Laser (top panel) and GPR (bottom panel) profile data of a 2.5 km line section adjacent to but overlapping with the section of Figure 3.7 showing numerous melt ponds in thin ice

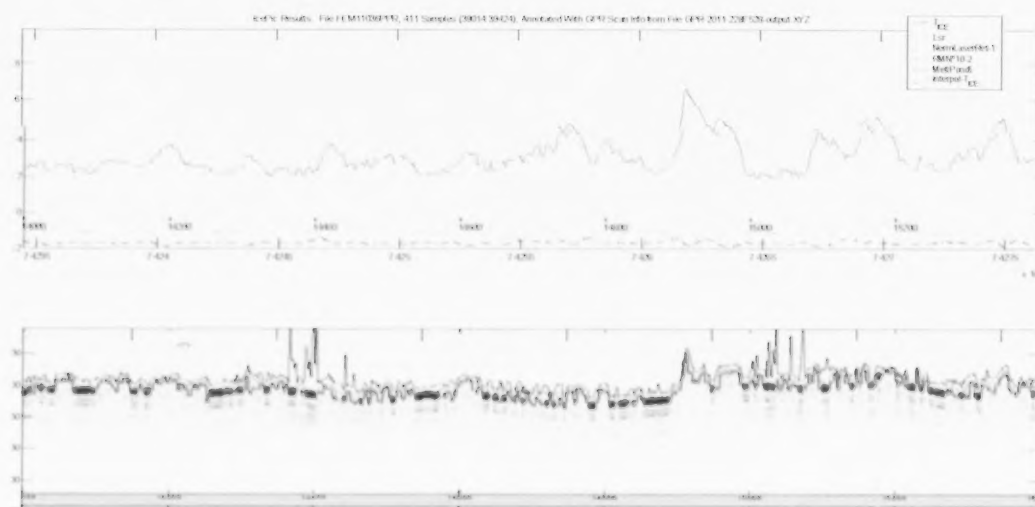


Fig. 3.9 EM-Laser (top panel) and GPR (bottom panel) profile data of a 2.5 km line section adjacent to the section of Figure 3.8 showing numerous melt ponds in thin ice.

3.4 CONCLUSIONS

The laser data collected along low flying ice survey lines used to determine the EM ice+snow thicknesses can also provide through its brightness channel estimates of the location and extent of melt ponds. Thus with additional analysis of the laser brightness data, the laser sensor provides additional pack ice information without introducing an additional sensor. The presence of melt ponds and in particular those where the freshwater is not mixed with the ocean surface layer either by having an ice bottom or due to the lack of wave generated vertical mixing for bottomless melt ponds, causes the EM inferred ice+snow thickness to include also the fresh water of the melt pond. Thus the inferred "ice thickness" referred to in the summer 2011 MY melting pack ice of the Canadian Beaufort Sea consisted of the total surface layer thickness of ice+snow+meltwater.

The additional information on the melt pond distribution from the laser brightness data can assist in the interpretation of the "ice thickness" histograms for ice thickness bins of less than 4 m where an ice thickness peak appeared in the summer 2011 data and interpreted as being caused by the numerous melt ponds within the summer MY pack ice. The ice thicknesses greater than 4 m in the summer 2011 data mostly represent true solid ice with the occasional bottomless small melt pond included into the inferred thickness.

There appears to be a good visual spatial distribution correlation between the EM's laser brightness data and the GPR echo strength data. Thus both data sets are capable to identify the distribution of melt ponds; numerically the Laser brightness data provided a higher density value than the GPR echo strength data even though the laser does has

missing data, but this we feel is caused by the three point averaging of the GPR echo data which eliminates a lot of the small melt ponds as well as decreases the size of the large melt ponds. Further field and analysis work will be needed to enhance the accuracy of the frequency of melt ponds within summer melting pack ice as provided by the Laser and GPR brightness data and determine the size limitation of melt ponds these techniques can provide.

4.0 CONCLUSIONS

The sea ice survey over the MY ice pack of the Canadian Beaufort Sea in the summer of 2011 provided a unique data set to investigate if the existing helicopter-borne sensors could identify the melt pond distribution in the decaying pack ice. The presence of melt ponds not mixed with the ocean surface layer either by having an ice bottom or due to the lack of vertical mixing for bottomless melt ponds, causes the EM ice+snow thickness determination to include the melt ponds in the summer melting pack ice in their inferred "ice thickness" distribution.

It was found that the laser data that is required to determine the EM ice+snow thicknesses can also be used to provide through its brightness channel estimates of the location and extent of melt ponds along the low flying ice survey lines as seen using the summer 2011 MYI survey data from the Canadian Beaufort Sea. The laser brightness data analysis thus would provide additional pack ice information without introducing an additional sensor. The melt pond distribution from the laser brightness data can assist in the interpretation of the "ice thickness" histograms. As seen in the summer 2011 data, the ice thickness peak appears at a thickness of less than 4 m and in part is caused by the occurrences of the numerous melt ponds within the summer MY pack ice.

Similarly, the use of the GPR data for melt pond analysis provides an additional capability for the GPR beyond its original role to monitor snow depths over sea ice. This is particularly useful as in late summer melt ponds occur while any remaining snow would be too wet for successful GPR snow depth measurements. Using the number of scans that identify melt ponds versus the total number of scans of the track's profile provide the best and simplest way to obtain the concentration of melt ponds along the flight track.

There appears to be a good visual correlation between the spatial distribution of the EM's laser brightness data and the GPR echo strength data. Thus both data sets appear to be able to identify the distribution of melt ponds. Numerically the Laser brightness data provided a higher melt pond frequency value in spite of missing data due to the "Laser Mirror effect" than the GPR echo strength data but this we feel is caused by the three point averaging of the GPR echo data which eliminates a lot of the small melt ponds as well as decreasing the size of the large melt ponds.

The video image processing results are visually appealing, but due to the fact the Video data sets (Video versus EM/GPR) are not collected simultaneously with the ice thickness data and due to the presence of ice drift and rotation there is difficulty aligning the video data collected at high altitude accurately with the GPR and Laser data collected at low altitude. Both GPR brightness and video methods do provide however an estimation of the melt pond occurrence within the pack ice although one being derived from a narrow line data file while the other covers a swath width of over 50m.

All three methods, Laser brightness, GPR echo strength, and Video white colour, show great potential to determine the melt pond frequency in summer multi-year pack ice, but

further field and analysis work is required to refine each method so that they will provide the same numerical melt pond frequency values as well as provide information on the size limit of melt ponds these techniques can provide.

5.0 ACKNOWLEDGEMENTS

The authors would like to thank Canadian Coast Guard Helicopter pilot Robert Pelletier and Engineer Eddy Perron for their assistance during the survey. In particular CCG pilot Bob Pelletier is thanked for the smooth flying at low altitude even in tasking weather conditions. The authors also thank John Iacozza and Simon Higginson for reviewing the report. The work was supported by the Program of Energy and Development and through Centre of Environmental Observation Sciences (CEOS, Prof. David Barber) that manage the large survey contract of ArcticNet with ExxonMobil covering the 2011 sea ice survey.

6.0 REFERENCES

- Lalumiere, L., S. Prinsenberg and I. Peterson, 2000. Observing Pack Ice Properties with a Helicopter-Borne-Laser-GPS Sensor. In Proceedings of the Tenth (2000) International Offshore and Polar Engineering Conference, Seattle, USA, May 28-June 2, 2000, Vol. I, pp.697-703.
- Lalumiere, L. and S. Prinsenberg, 2009. Integration of a Helicopter-Based Ground Penetrating Radar (GPR) with a Laser, Video and GPS System. In Proceedings of the Nineteenth (2009) International Offshore and Polar Engineering Conference Osaka, Japan, June 21-26, 2009, Vol. I, pp. 658-665.
- Lalumiere, L. 2011. GPR Capabilities for Ice Thickness sampling of Low Salinity Ice and for Detecting Oil-In-Ice. Can. Contractor Rep. of Hydrography and Ocean Sciences #56, iv+36.
- Prinsenberg, S.J., Ingrid Peterson and Scott Holladay, 2011. IOL Helicopter Survey Report 2011, Survey period August 11-25. Internal report for the Bedford Institute of Oceanography, 21pp.

APPENDIX 1: 2010 INTERNAL BIO REPORT

Laser Brightness Normalization Procedure to Determine Ice Cover Properties in the Gulf of St. Lawrence

L. Lalumiere

Sensors by Design Ltd., 217 Lorne Ave, Newmarket, Ontario, Canada L3Y 4K5

Abstract

A new laser altimeter unit added to the Bedford Institute of Oceanography's Video Sensor System has a feature which provides surface brightness measurement at near-infrared wavelengths. A technique was developed to use the altitude reading to remove the dependence of altitude in the brightness measurement. The laser altimeter provides an active source brightness measurement not dependent on the ambient lighting conditions. Brightness returns over sea ice with varying amounts of snow cover are examined. The goal for this sensor technology is the classification of the pack ice surface for ice, snow covered ice and open water conditions. Some ambient light near-infrared video images are provided.

Introduction

For the Winter 2001 field season a new laser altimeter was added to the Bedford Institute of Oceanography's Video Sensor System. The laser is mounted in a pod attached to the skid gear of a Canadian Coast Guard BO-105 helicopter. A video camera is also mounted in the pod. A laptop-based data acquisition system is used to log laser altimeter readings, capture digital video images, log GPS positions and log the helicopter's radar altimeter reading. Data presented were collected in the Hillsborough Bay, PEI and in the Northumberland Strait.

The new laser altimeter unit has a feature which provides a surface brightness reading. This report documents the initial work performed to determine if the laser brightness reading can provide useful information about ice cover conditions.

The laser brightness readings vary with surface conditions and with altitude. The laser brightness data were analyzed to determine if a normalization procedure could be developed to remove the variations in brightness readings caused by altitude changes. Surface conditions as recorded with the on-board video camera are also presented.

The laser operates at a near-infrared wavelength. To provide additional information on how the ice surface conditions appear at near-infrared wavelengths, some example video images from a near-infrared sensitive cam-corder are provided.

Laser System

The laser is an Optech 3-Alpha Geophysical laser range-finder. The laser has an infrared beam operating at 905 nm. The laser manual reports the laser footprint up to ranges of 20 m (at 1 m the footprint is 0.045 m at 20 m the footprint is 0.14 m). Scaling for higher operating altitudes:

- at 50 m the beam width is 0.290 m
- at 100 m the beam width is 0.540 m
- at 200 m the beam width is 1.040 m

The laser has a pulse repetition rate of 2000 Hz. Altitude readings are produced at a rate of 30 Hz. For each reading a large percentage of received pulses are used to determine altitude and a small percentage are used to determine the brightness of the received pulses.

The Video Sensor System's video image footprint is approximately the same as the flying height. At 50 m altitude the surface pixel size is approximately 15 to 17 cm. So the laser footprint is about 4 adjacent pixels.

The laser is an optical device and we are measuring the reflectance of light at the near-IR frequency of the laser. The laser altimeter is an active device, so the level of near-IR from the sun must be at or below the noise floor of the laser receiver. As a result, we are measuring the reflectance of the near-IR light independent of daylight conditions.

Field Data

Lift Tests

The two lift tests over ice and snow were used to look at the brightness variation versus altitude. The file with the data collected over white snow is D2001_040-F034 and the file with the data file collected over ice is D2001_040F032. The data collection was performed on February 9, 2001 in Hillsborough Bay, PEI. The test over snow (Fig. 1) provided a more uniform surface during the test and the plot shows less noise than the test over ice (Fig. 2) (there was some snow present on the ice).

Appendix A shows the normalization results from two additional lift tests performed on March 22, 2001.

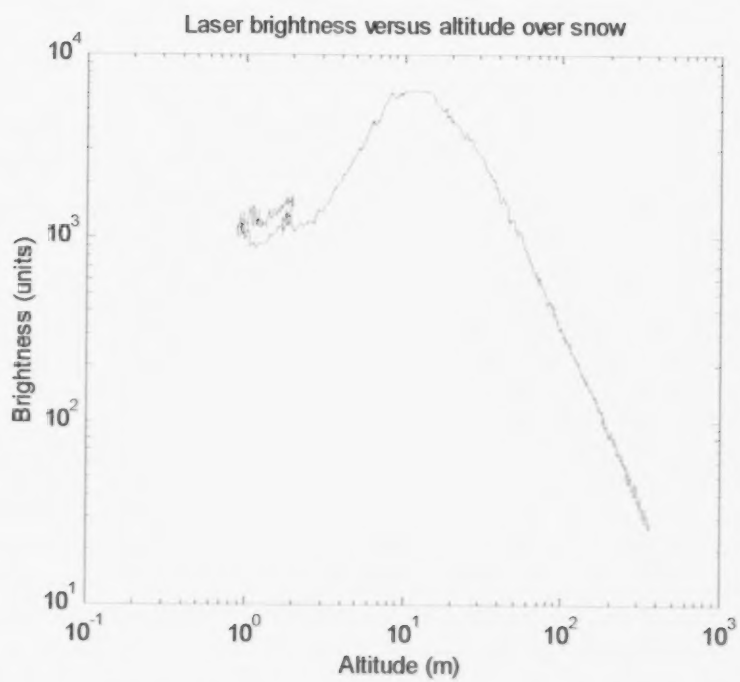


Fig. 1 Lift test over snow

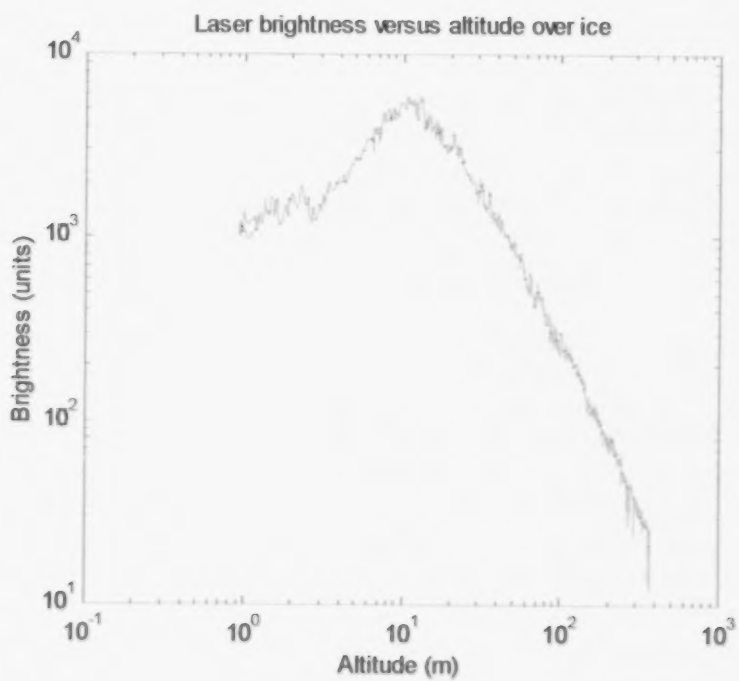


Fig. 2 Lift test over ice

The area of linearity in the log-log plot extends from approximately 30 m to higher altitudes. This might be due to non-linearity in the laser's receiver as the signal level nears saturation when the surface is near to the laser altimeter.

Brightness readings in the linear area of the snow lift test were taken and a brightness function dependent on altitude was created. The brightness reading used at 50 m altitude was 1200 and the brightness reading used at 350 m altitude was 29. The resulting normalization equation is shown in Equation 1.

$$\text{NormalizedBrightness} = \frac{\text{LaserBrightness}}{10^{(-1.91313 \times \text{Log}_{10}(\text{LaserAltitude}) + 6.3295)}} \quad (\text{Equation 1})$$

Figure 3 shows the results of the snow lift test data after normalization using Equation 1. Figure 4 shows the results of the ice lift test data after normalization using the equation derived with the snow lift test data.

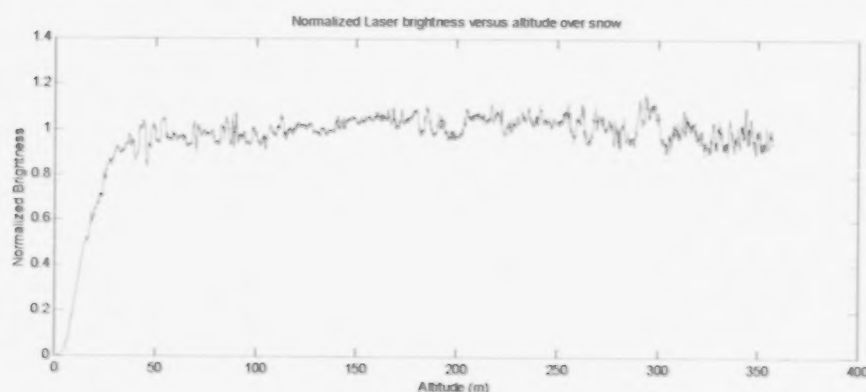


Fig. 3 The results of the snow lift test data after normalization

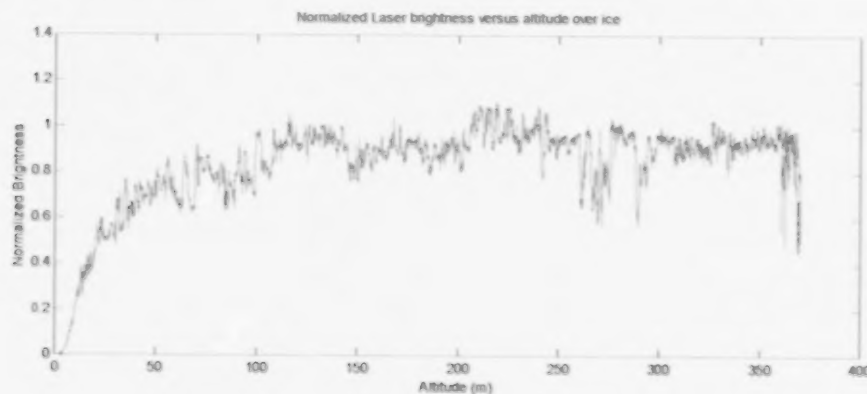


Fig. 4 The results of the ice lift test data after normalization (using the snow derived function)

The ice lift test data does not map to one down to 30 or 40 m like the snow lift data. The divergence starts around 100 m altitude. The helicopter drifted towards the west during this test and the ice cover may have changed.

Surface Conditions

An area with a good variety of ice brightness with snow and nearby open water was selected to study the laser brightness response. Black plastic bags were placed in a grid over the area so that helicopter survey lines could be flown with overlapping coverage and at different altitudes. Two lines were studied for this report, lines at 50 m and 100 m over the center of the gridded area. A still photo is shown in Figure 5. The photograph does not show the white snow cover at the start of each profile but the bags can be seen on the ice.

The file with the data collected at 50 m altitude is D2001_040F025 and the file with the data file collected at 100 m altitude is D2001_040F029. The data collection was performed on February 9, 2001 in Hillsborough Bay, Prince Edward Island. The 50 m altitude line is 924 m long and approximately 50 m wide. The 100 m altitude line is 1525 m long and approximately 100 m wide. The surface coverage of the 50 m altitude line is contained within the 100 m altitude line starting approximately 200 m from the start of the 100 m line and ending approximately 500 from the end of the 100 m line.

Table 1 lists the changing surface conditions along the line flown at 50 m altitude. Table 2 lists the changing surface conditions along the line flown at 100 m altitude. Mosaics of the video frames for the two lines were created using the Video Viewer program. Figure 6 shows the video frame mosaic for the 50 m altitude line. Figure 7 shows the video frame mosaic for the 100 m altitude line. For the surface descriptions given in Tables 1 and 2, approximate video frame numbers corresponding to the video mosaics are shown in Figures 6 and 7. The tables also provide approximate sample number positions for comparisons with the profile plots shown in Figures 8 to 11.

Table 1 Description of surface conditions for the 50 m altitude line

Surface Description	Approximate Video Frame Range	Approximate Laser Profile Sample Number Range
Fairly uniform snow cover	1 to 14	1 to 100
Ice with varying patches of snow	15 to 74	100 to 800
5-10 m of snow cover up to a ridge	74	800
Rough ice with lots of snow cover	75 to 108	800 to 1250
Broken up ice	108 to 120	1250 to 1400
Dark ice floe	120 to 175	1400 to 2000
Some ridging	176 to 180	2000 to 2100
Second floe	181 to end	2100 to the end

Table 2 Description of surface conditions for the 100 m altitude line

Surface Description	Approximate Video Frame Range	Approximate Laser Profile Sample Number Range
Fairly uniform snow cover	1 to 39	1 to 450
Ice with varying patches of snow	40 to 85	450 to 1000
5-10 m of snow cover up to a ridge	86	1000
Rough ice with lots of snow cover	87 to 123	1000 to 1500
Broken up ice	124 to 134	1500 to 1650
Dark ice floe	135 to 164	1650 to 2000
Some ridging	165 to 167	2000 to 2100
Second floe	168 to 205	2100 to 2500
Beyond coverage of 50 m altitude line	170 to end	2200 to end
Brighter ice	205 to 222	2500 to 2700
White ice ridge	223 to 229	2700 to 2750
Thin rafted ice or broken up thin ice	230 to end	2750 to the end



Fig. 5 Photograph of survey line flown at 50 and 100 m

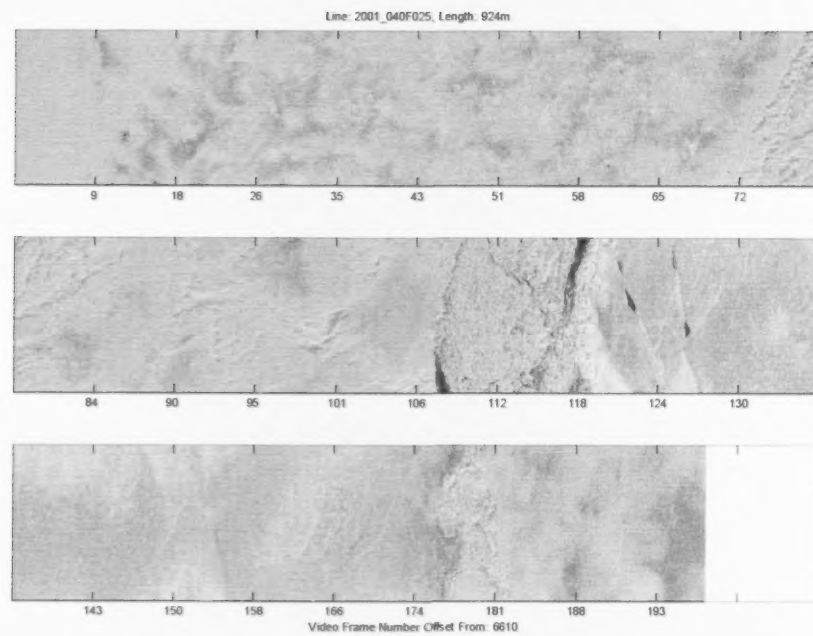


Fig. 6 The video image mosaic for the 50 m altitude line.

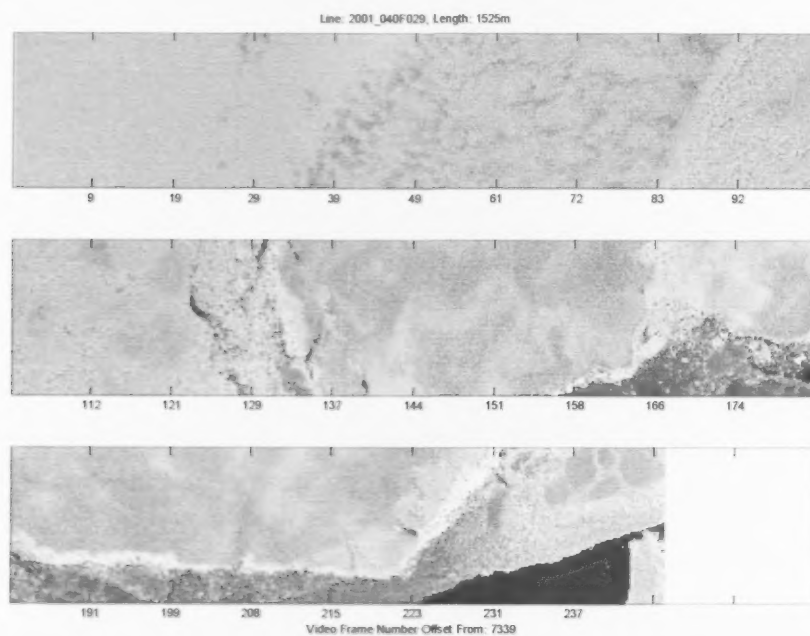


Fig. 7 The video image mosaic for the 100 m altitude line.

Raw Laser Altimeter Data

Figure 8 shows the profile plots for the laser altimeter altitude and raw brightness readings for the 50 m altitude line. Figure 9 shows the profile plots for the laser altimeter altitude and raw brightness readings for the 100 m altitude line.

Though the 50 m and 100 m lines do not match exactly, there is very good match for the normalized values over the expected surface conditions along the profiles. The range of brightness values for the 50 m line vary from approximately 1600 down to approximately 100. The range of brightness values for the 100 m line vary from approximately 350 down to approximately 30 (not including the end of the 100 m line which was not covered with the 50 m line).

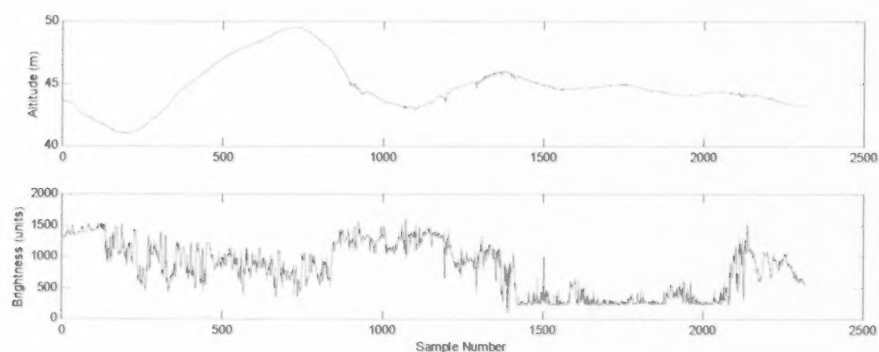


Fig. 8 The raw brightness profile for the 50 m line.

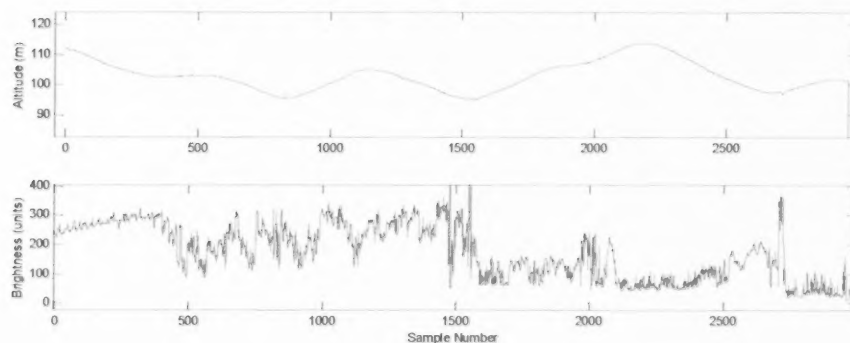


Fig. 9 The raw brightness profile for the 100 m line.

Normalized Laser Brightness Results

Figure 10 shows the normalized brightness profile for the 50 m altitude line and Figure 11 shows the normalized brightness profile for the 100 m altitude line.

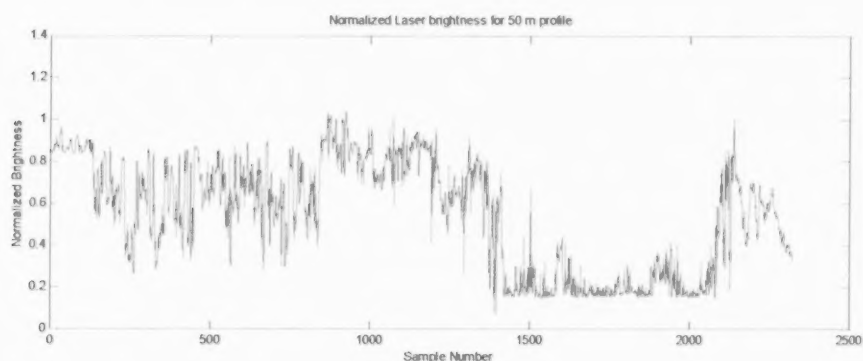


Fig. 10 The normalized brightness profile for the 50 m line.

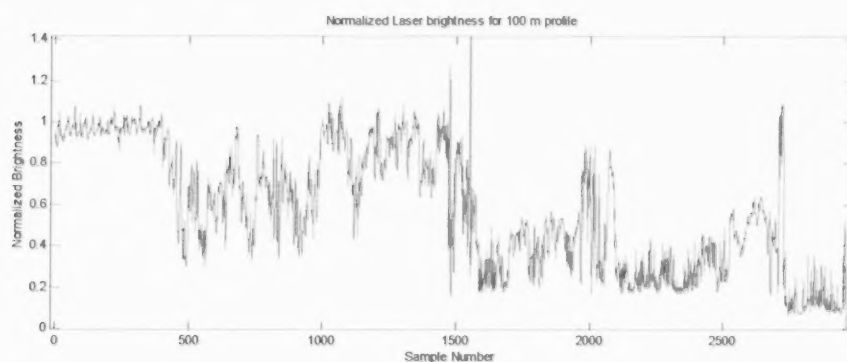


Fig. 11 The normalized brightness profile for the 100 m line.

After normalization, the surface returns over the regions common to both lines varied from approximately 1 down to 0.1. The fairly uniform snow cover has a normalized result of approximately 1.0. Ice with varying patches of snow has a normalized result ranging from approximately 0.3 to 1.0. The area of rough ice with lots of snow cover has a normalized result ranging from approximately 0.5 to 1.0. For the last part area of common coverage in both lines (the dark ice floe) the normalized brightness reading is generally near 0.2 with some readings up to 0.4 for the 50 m altitude line and a varying reading between 0.2 and 0.4 for the 100 m altitude line.

The area from sample number 2000 to the end of the 100 m line does not have a corresponding area in the 50 m line.

Cam-corder Images of Ice and Open Water

For evaluating the laser results, the closest we can come with an imaging system that "sees" a similar view as the laser brightness would be a Sony cam-corder with the Night-Shot feature. This camera with a near infrared-pass only filter will show the near-IR reflectance of the surface. These images will vary with cloud cover and exposure settings of the camera. Recordings from a Sony cam-corder with the Night-Shot feature and a near-infrared-pass only filter were taken over the ice in the Northumberland Strait in 1999.

A comparison of the normal video recording and the infrared-pass-only recording is shown in Appendix B. The images shown in Appendix A are arranged with the visible light images in the left column and infrared-pass-only images in the right column. Each row has shows ice conditions seen within a few seconds of each other from the helicopter. For some frame pairs, the visible light image was collected before the infrared-pass-only image and for some frames it was the other way around. The infrared-pass-only frames show more contrast in the ice with this ice appearing dark and snow appearing bright white. These images were collected using a hand-held cam-corder with a variable zoom lens and as a result the scale of these images cannot be accurately determined.

Conclusions

While the laser brightness readings for a given surface do vary with altitude of the laser from the surface, this variation can be removed. The laser altimeter itself provides the altitude information needed to correct for the brightness signal losses with increased altitude. For the data examples processed to-date the normalization has worked quite well.

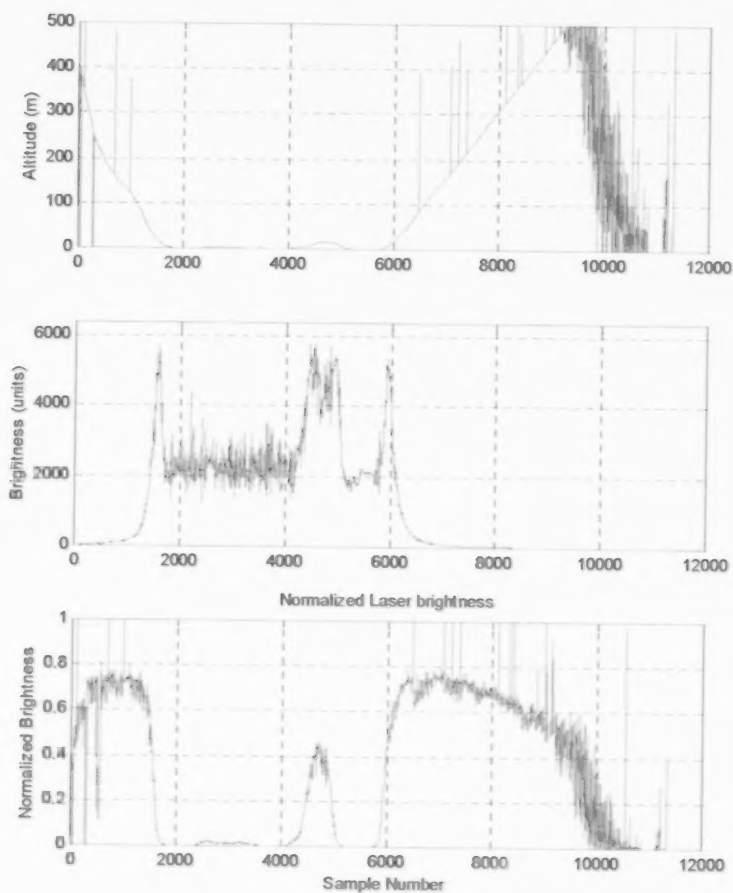
The end goal for the developing a successful technique to normalize the laser brightness readings is to classify the surface coverage as snow covered, ice covered or open water. Further work is needed to process the available data collected with the Video Sensor System to determine a classification process and the likely success of this approach.

The normalization function used here was derived empirically. Further work to develop a function based on the appropriate theory for light scattering and spreading losses will undoubtedly increase the robustness of the reported results.

Appendix A - Other Normalized Laser Brightness Plots

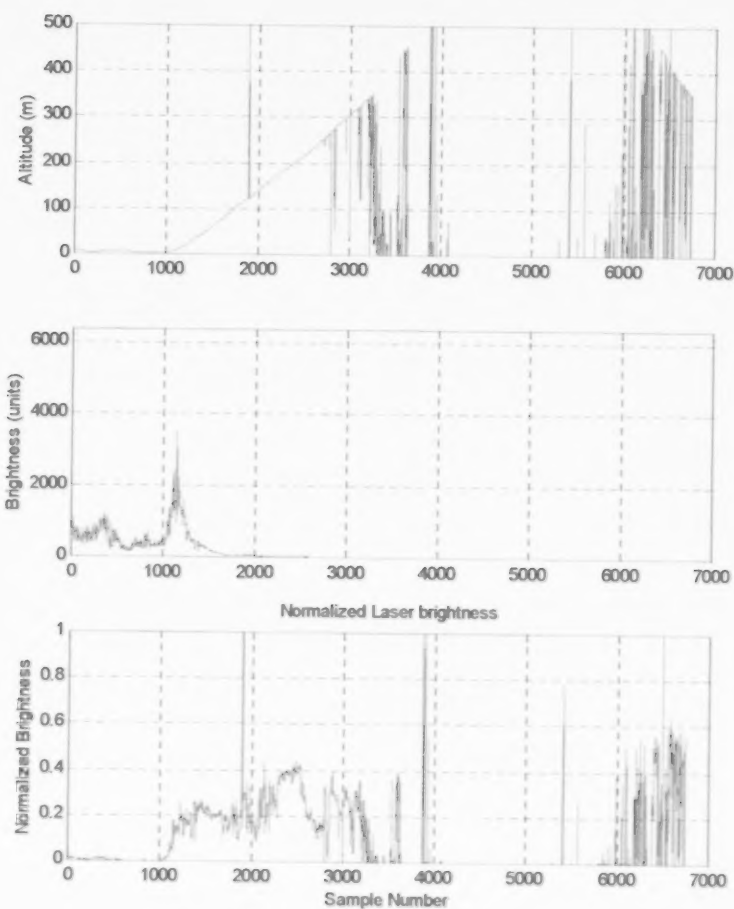
The laser altimeter altitude and brightness readings from two additional lift tests over ice were analyzed. The same normalization function was applied as that used in the main report figures. Each plot shows the altitude, the raw brightness reading and the normalized brightness reading.

For the 076 flight the normalized reading stays with a range of 0.1 from approximately 20m to over 300 m on the going up segment. This line is shown in Plot 1.




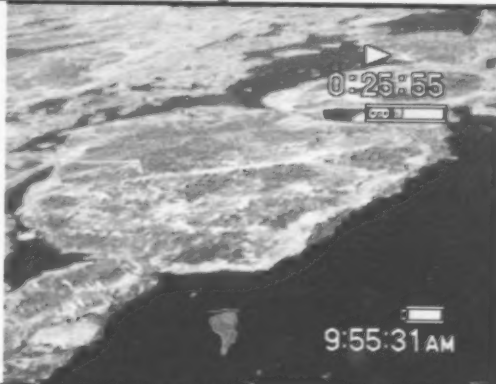



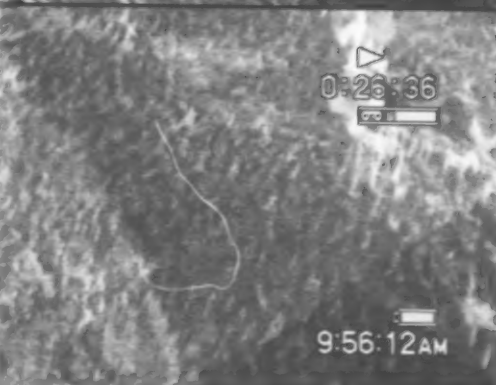
Plot 1 D2001_076F126_laser

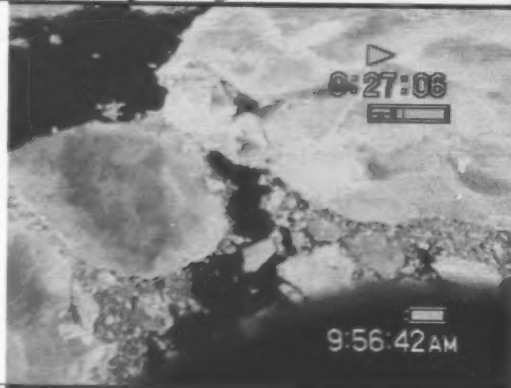
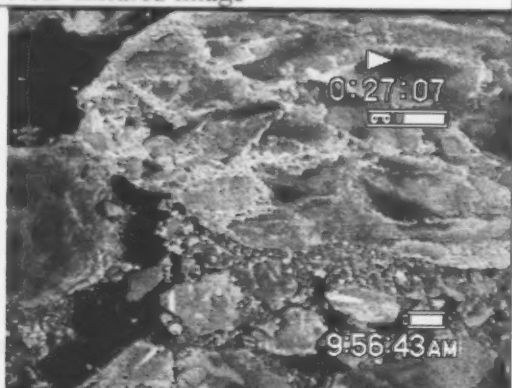

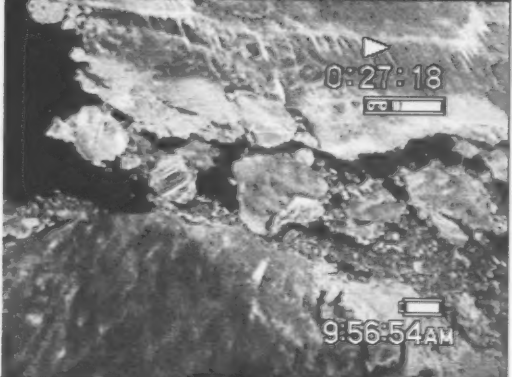

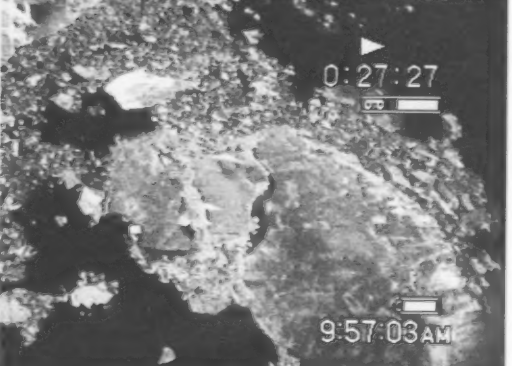
For the 081 flight, from about 75 to about 170 m the reading seems noisy then above 170 there seems to be a change in the normalized reading hovering at about 0.4.



Plot 2 D2001_081F338_laser

Appendix B - Cam-corder Visible Light and Near-infrared Images.

	Visible Light Image	Near-Infrared Image
1	 A grayscale visible light image showing a coastal or riverine landscape. A dark, irregular shape, possibly a boat or a shadow, is in the lower right. A timestamp '0:25:59' with a play icon and a battery level indicator are in the upper right. A timestamp '9:55:35 AM' with a battery level indicator is in the lower right.	 A grayscale near-infrared image of the same scene as Visible Light Image 1. The dark shape in the lower right is more pronounced. A timestamp '0:25:55' with a play icon and a battery level indicator are in the upper right. A timestamp '9:55:31 AM' with a battery level indicator is in the lower right.
2	 A grayscale visible light image showing a different landscape, possibly a field or a body of water with reeds. A timestamp '0:26:21' with a play icon and a battery level indicator are in the upper right. A timestamp '9:55:57 AM' with a battery level indicator is in the lower right.	 A grayscale near-infrared image of the same scene as Visible Light Image 2. The features are more textured. A timestamp '0:26:19' with a play icon and a battery level indicator are in the upper right. A timestamp '9:55:56 AM' with a battery level indicator is in the lower right.
3	 A grayscale visible light image showing a landscape with a large, light-colored, irregular shape, possibly a cloud or a large object. A timestamp '0:26:37' with a play icon and a battery level indicator are in the upper right. A timestamp '9:56:13 AM' with a battery level indicator is in the lower right.	 A grayscale near-infrared image of the same scene as Visible Light Image 3. The light-colored shape is more defined. A timestamp '0:26:36' with a play icon and a battery level indicator are in the upper right. A timestamp '9:56:12 AM' with a battery level indicator is in the lower right.

	Visible Light Image	Near-Infrared Image
4	 <p>0:27:06</p> <p>9:56:42AM</p>	 <p>0:27:07</p> <p>9:56:43AM</p>
5	 <p>0:27:20</p> <p>9:56:56AM</p>	 <p>0:27:18</p> <p>9:56:54AM</p>
6	 <p>0:27:29</p> <p>9:57:05AM</p>	 <p>0:27:27</p> <p>9:57:03AM</p>